

GA-NIFS: interstellar medium properties and tidal interactions in the evolved massive merging system B14-65666 at $z = 7.152$

Gareth C. Jones^{1,2,3*}, Rebecca Bowler⁴, Andrew J. Bunker¹, Santiago Arribas⁵, Stefano Carniani⁶, Stephane Charlot⁷, Michele Perna⁵, Bruno Rodríguez Del Pino⁵, Hannah Übler^{2,3,8}, Chris J. Willott⁹, Jacopo Chevallard¹, Giovanni Cresci¹⁰, Eleonora Parlanti⁶, Jan Scholtz^{2,3}, Giacomo Venturi⁶

¹ Department of Physics, University of Oxford, Denys Wilkinson Building, Keble Road, Oxford OX1 3RH, UK

² Kavli Institute for Cosmology, University of Cambridge, Madingley Road, Cambridge CB3 0HA, UK

³ Cavendish Laboratory, University of Cambridge, 19 JJ Thomson Avenue, Cambridge CB3 0HE, UK

⁴ Jodrell Bank Centre for Astrophysics, Department of Physics and Astronomy, School of Natural Sciences, The University of Manchester, Manchester, M13 9PL, UK

⁵ Centro de Astrobiología (CAB), CSIC-INTA, Ctra. de Ajalvir km 4, Torrejón de Ardoz, E-28850, Madrid, Spain

⁶ Scuola Normale Superiore, Piazza dei Cavalieri 7, I-56126 Pisa, Italy

⁷ Sorbonne Université, CNRS, UMR 7095, Institut d'Astrophysique de Paris, 98 bis bd Arago, 75014 Paris, France

⁸ Max-Planck-Institut für extraterrestrische Physik (MPE), Gießenbachstraße 1, 85748 Garching, Germany

⁹ NRC Herzberg, 5071 West Saanich Rd, Victoria, BC V9E 2E7, Canada

¹⁰ INAF - Osservatorio Astrofisico di Arcetri, largo E. Fermi 5, 50127 Firenze, Italy

Accepted XXX. Received YYY; in original form ZZZ

ABSTRACT

We present JWST/NIRSpec IFU observations of the $z = 7.152$ galaxy system B14-65666, as part of the GA-NIFS survey. Line and continuum emission in this massive system ($\log_{10}(M_*/M_\odot) = 9.8 \pm 0.2$) is resolved into two strong cores, two weaker clumps, and a faint arc, as seen in recent JWST/NIRCam imaging. Our dataset contains detections of [OII] $\lambda\lambda 3726, 3729$, [NeIII] $\lambda\lambda 3869, 3968$, Balmer lines (H β , H γ , H δ , H ϵ , H ζ), [OIII] $\lambda\lambda 4959, 5007$, and weak [OIII] $\lambda 4363$. Each spectrum is fit with a model that consistently incorporates interstellar medium conditions (i.e., electron temperature, T_e , electron density, n_e , and colour excess, $E(B - V)$). The resulting line fluxes are used to constrain the gas-phase metallicity ($\sim 0.3 - 0.4$ solar) and H β -based SFR ($310 \pm 40 M_\odot \text{ yr}^{-1}$) for each region. Common line ratio diagrams (O32-R23, R3-R2, Ne3O2-R23) reveal that each line-emitting region lies at the intersection of local and high-redshift galaxies, suggesting low ionisation and higher metallicity compared to the predominantly lower-mass galaxies studied with the JWST/NIRSpec IFU so far at $z > 5.5$. Spaxel-by-spaxel fits reveal evidence for both narrow (FWHM $< 400 \text{ km s}^{-1}$) and broad (FWHM $> 500 \text{ km s}^{-1}$) line emission, the latter of which likely represents tidal interaction or outflows. Comparison to ALMA [C II] $158\mu\text{m}$ and [O III] $88\mu\text{m}$ data shows a similar velocity structure, and optical-far infrared diagnostics suggest regions of high Lyman continuum escape fraction and n_e . This source lies on the mass-metallicity relation at $z > 4$, suggesting an evolved nature. The two core galaxies show contrasting properties (e.g., SFR, M_* , Z_g), suggesting distinct evolutionary pathways. Combining the NIRSpec IFU and ALMA datasets, our analysis opens new windows into the merging system B14-65666.

Key words: galaxies: high-redshift – galaxies: interactions – galaxies: ISM – galaxies: kinematics and dynamics

1 INTRODUCTION

The first 1 Gyr of the Universe ($z > 6$) was a unique era of cosmic time. The first galaxies emerged (e.g., Laporte et al. 2021; Curtis-Lake et al. 2023; Carniani et al. 2024a) and started the process of ionising their surroundings (e.g., Nakajima et al. 2023; Bañados et al. 2018). Galaxy formation was rapid and fruitful, with high galaxy merger rates (e.g., Duan et al. 2024), and evidence for increasing volume density of molecular gas (e.g., Riechers et al. 2019; Aravena et al. 2024; Ragone-Figueroa et al. 2024) and star formation rate (SFR; e.g., Gruppioni et al. 2020; Khusanova et al. 2021; Traina

et al. 2024) with increasing cosmic time, based on extrapolation from $3 < z < 6$.

The first $z > 6$ galaxies were detected less than three decades ago (e.g., Fan et al. 2001; Hu et al. 2002; Stanway et al. 2003; Taniguchi et al. 2005), but through the advent of cutting edge telescopes, the redshift frontier has already been extended to within the first ~ 300 Myr of the Universe ($z > 13$; e.g., Carniani et al. 2024b; Kokorev et al. 2024; Witstok et al. 2024). Morpho-kinematic studies of high-redshift galaxies with ALMA revealed a population of relaxed rotating disk galaxies (e.g., Neeleman et al. 2020; Lelli et al. 2021; Herrera-Camus et al. 2022; Rowland et al. 2024), but many observations revealed clumpy or merging systems (e.g., Carniani et al. 2018; Jones et al. 2021). This was supported by the results of zoom-in

* E-mail: gj283@cam.ac.uk

cosmological simulations, which showed that bright $z > 6$ galaxies accreted mass through frequent interactions with lower-mass satellites and/or collisions (e.g., Kohandel et al. 2019; Pallottini et al. 2022). However, most spectroscopic ALMA observations featured low spatial resolution ($\sim 1''$, corresponding to ~ 6 kpc at $z = 6$).

This picture was made even clearer with the advent of JWST (Gardner et al. 2023) and the integral field unit (IFU) on the NIRSpec instrument (Böker et al. 2022; Jakobsen et al. 2022). With a narrow point spread function ($\sim 0.1 - 0.2''$ or $0.6 - 1.2$ kpc at $z = 6$; D’Eugenio et al. 2024b), the NIRSpec IFU is able to map multiple bright rest-UV and rest-optical lines at $z > 4$ (e.g., H α , [OIII] $\lambda\lambda 4959, 5007$). While JWST follow-up observations of some galaxies classified as rotators based on previous rest-frame far-infrared (FIR) observations confirmed their nature (e.g.; ALESS73.1, Lelli et al. 2021; Parlanti et al. 2024b; GN20, Hodge et al. 2012; Übler et al. 2024b), other galaxies were found to feature clumpy morphologies, close companions, and sometimes outflows (e.g.; HZ10, Jones et al. 2017, 2024a; HZ4, Herrera-Camus et al. 2022; Parlanti et al. 2024a; COS3018, Smit et al. 2018; Scholtz et al. 2024). Due to the detection of multiple emission lines, these data were used to map morphology, kinematics, and the interstellar medium (ISM) conditions (e.g., electron density n_e and temperature T_e , and gas-phase metallicity Z_g) of each target.

A number of JWST/NIRSpec IFU observations have already detailed the properties of $z > 6$ galaxies (e.g., Hashimoto et al. 2023a; Decarli et al. 2024; Fujimoto et al. 2024; Liu et al. 2024; Lyu et al. 2024; Messa et al. 2024; Scholtz et al. 2024; Venturi et al. 2024). Many of these have been acquired as part of the Galaxy Assembly with NIRSpec Integral Field Spectroscopy (GA-NIFS)¹ Guaranteed Time Observation (GTO) survey (Cycles 1 and 3; PIs R. Maiolino & S. Arribas; e.g. Marshall et al. 2023, 2024; Arribas et al. 2024; Jones et al. 2024b; Marconcini et al. 2024b,a; Scholtz et al. 2024; Übler et al. 2024a). This survey, which includes 55 targets between $2 < z < 11$, was designed to exercise the power of the NIRSpec IFU through observations of a variety of well-studied galaxies (e.g., star-forming galaxies, active galactic nucleus [AGN] host galaxies, quasars). In this work, we present the GA-NIFS observations of the $z \sim 7.152$ Lyman break galaxy (LBG) B14-65666.

A key factor in the discovery of B14-65666 was the Ultra Deep Survey with the VISTA (Visible and Infrared Survey Telescope for Astronomy; Emerson & Sutherland 2010) telescope (UltraVISTA; McCracken et al. 2012), which targeted the COSMOS field (Scoville et al. 2007) in Y , J , H , and K_s near-infrared bands. Combining UltraVISTA DR1 with other optical and infrared data, Bowler et al. (2012) first reported B14-65666 as one of only four robust $z > 6.5$ galaxies from a sample of $> 2 \times 10^5$ detected sources. Bowler et al. (2014) performed a follow-up photometric SED modelling analysis combining UltraVISTA DR2 and additional data, improving the accuracy of the photometric redshift of this source.

The first resolved image of this source was taken with HST/WFC3 F140W (Bowler et al. 2017), where two closely separated clumps (aligned nearly east-west) are visible. ALMA follow-up observations of the source were first performed in Bowler et al. (2018), where B14-65666 was the only dust continuum detected source in Band 6 in a sample of six luminous LBGs. Hashimoto et al. (2019) confirmed the dust continuum detection and morphology of this source. In addition, they detected the spatially resolved [C II] $\lambda 158\mu\text{m}$ ($L_{[\text{CII}]158\mu\text{m}} = (11.0 \pm 1.4) \times 10^8 L_\odot$) and [O III] $\lambda 88\mu\text{m}$ ($L_{[\text{OIII}]88\mu\text{m}} = (34.4 \pm 4.1) \times 10^8 L_\odot$) FIR lines, which provided

spectroscopic redshift confirmation ($z_{\text{sys}} = 7.1520 \pm 0.0003$)². Modelling of the two-point dust SED yielded $T_{\text{dust}} \sim 50 - 60$ K and $L_{\text{FIR}} \sim 10^{12} L_\odot$. The dust continuum emission appears to be elongated, potentially aligned with the two components (see also Bowler et al. 2022 who find the dust to be between the two UV clumps). Based on these properties, Hashimoto et al. suggest that B14-65666 is a merger-driven starburst.

Follow-up ALMA observations did not return a significant [N II] $\lambda 122\mu\text{m}$ emission ($< 8.1 \times 10^7 L_\odot$), but strong underlying FIR continuum emission (Sugahara et al. 2021). Detailed dust SED modelling returned similar T_{dust} and L_{FIR} constraints as Hashimoto et al. (2019), with an additional estimate on the dust mass of $M_{\text{dust}} \sim 10^7 M_\odot$. Similarly, ALMA observations of reliable molecular gas tracers (CO(7-6), CO(6-5), [C I](2-1)) and their underlying dust continuum emission resulted in non-detections (Hashimoto et al. 2023a). The molecular gas mass estimates implied by these non-detections are in agreement with the mass found through scaling relations based on the detection of [C II] $\lambda 158\mu\text{m}$ (Madden et al. 2020), FIR continuum emission (Li et al. 2019), and the kinematics of the [C II] $\lambda 158\mu\text{m}$ emission (Hashimoto et al. 2019): $M_{\text{mol}} = 10^{8.7-11.0} M_\odot$.

Most recently, Sugahara et al. (2024) have presented JWST/NIRCam imaging of B14-65666, as part of the ‘Reionization and the ISM/Stellar Origins with JWST and ALMA’ (RIOJA) project (JWST GO1 PID1840; PIs: J. Álvarez-Márquez and T. Hashimoto; Hashimoto et al. 2023b). From the flux excess between the F356W and F444W bands they infer the presence of strong [OIII] $\lambda 5007$ emission (rest-frame equivalent widths of 1000–2000 Å; as expected from the observed Spitzer colours; Bowler et al. 2014). Interestingly, the inferred [OIII] $\lambda 5007$ emission peaks in the Eastern component of the source, where the rest-frame UV emission is weaker. Through SED fitting of the resolved NIRCam and ALMA multi-band fluxes, Sugahara et al. (2024) derive a stellar mass of $\log_{10}(M_\star/M_\odot) = 9.78^{+0.16}_{-0.18}$ and a relatively low metallicity of $(Z_\star/Z_\odot) = 0.21^{+0.05}_{-0.04}$. The extremely high spatial resolution of the NIRCam data reveals that the Eastern component is compact, while the Western component is spatially resolved. Additional low surface brightness features are identified as tidal tails.

In this work, we exploit NIRSpec IFU observations from 2.9–5.3 μm to directly map the strength of the rest-frame optical emission lines across the source. In Section 2, we describe both our new JWST/NIRSpec IFU data for B14-65666 as well as archival data explored in this work. The NIRSpec data are then analysed in Section 3. We interpret and discuss these results in Section 4 and conclude in Section 5. We use a standard concordance cosmology (i.e., $H_0 = 70 \text{ km s}^{-1} \text{ Mpc}^{-1}$, $\Omega_m = 0.3$, $\Omega_\Lambda = 0.7$) throughout, where $0.1''$ corresponds to ~ 0.52 kpc at $z = 7.152$. A Chabrier (2003) initial mass function (IMF) with an upper mass limit of $100 M_\odot$ is assumed.

2 DATA DESCRIPTION

2.1 JWST/NIRSpec IFU

The data analysed here originated from GA-NIFS observations as part of project 1217 (PI: N. Luetzgendorf; details in Table 1). An eight-point ‘MEDIUM’ dither pattern was used, with a starting point of ‘1’. Data were taken at medium spectral resolution

² Because it was the first galaxy in the Epoch of Reionisation (EoR) with spatially resolved emission in three powerful tracers ([C II] $\lambda 158\mu\text{m}$, [O III] $\lambda 88\mu\text{m}$, and dust continuum emission), it was given the alternative alias of ‘Big Three Dragons’ after a combination of tiles in the game mahjong.

¹ <https://ga-nifs.github.io/>

Table 1. JWST NIRSpec/IFU observation properties.

Grating/Filter	G395M/290LP
Readout Pattern	NRSIRS2
Groups/Int	25
Ints/Exp	1
Exposures/Dithers	8
Total Time [ks]	14.7

(G395M/F290LP; $R \sim 1000$), covering $\lambda_{obs} = 2.871 - 5.270 \mu\text{m}$ ($\lambda_{rest} \sim 3522 - 6465 \text{ \AA}$ at $z = 7.1520$). No *leakcal* or background exposures were taken. The data were calibrated with the STScI pipeline (v1.15.0, CRDS 1241), with custom outlier rejection (D’Eugenio et al. 2024b), custom masks for contamination by cosmic ray strikes (‘snowballs’) and open MSA shutters leakage, 1/f noise corrections for count-rate maps, and drizzle weighting to create a data cube with spatial pixels (spaxels) of width $0.05''$ (see Perna et al. 2023 for full details of reduction).

Previous analyses of JWST/NIRSpec IFU data (e.g., Jones et al. 2024b; Parlanti et al. 2024a; Übler et al. 2024b) found astrometric errors due to the pointing accuracy of JWST ($\sim 0.1''$, Rigby et al. 2023). To determine if our data are affected by this error, we use available JWST/NIRCam imaging datasets that feature overlapping wavelength coverage (F356W and F444W; see Section 2.2 for details of these images). By convolving our IFU data cubes with the corresponding NIRCam filter transmission curves, we compare the spatial distribution of emission. The resulting comparisons are shown in the top row of Figure 1. It is clear that the NIRSpec IFU and NIRCam data are misaligned, with an average offset of $0.10 \pm 0.04''^3$. This is fully consistent with the pointing uncertainty of JWST, but to enable comparison with other datasets, we correct our NIRSpec IFU cube for this offset. The flux levels of the NIRSpec cube and NIRCam images agree (see Appendix A).

No background exposures were included in these observations, so we manually performed a background subtraction by extracting a mean spectrum from a large, signal-free area in the cube. This mean background spectrum was then subtracted from each spaxel.

Previous observations of high-redshift galaxies with the JWST/NIRSpec IFU revealed the presence of sinusoidal artefacts (‘wiggles’) in single-spaxel spectra (e.g., Perna et al. 2023; Decarli et al. 2024; Ulivi et al. 2024). These wiggles, which were caused by under-sampling of the PSF, were more noticeable for drizzled maps featuring bright point sources coincident with extended emission (i.e., AGN and QSOs). We have followed the procedure of Perna et al. (2023) to inspect our data for these wiggles, finding little evidence of strong wiggles in our data. While their presence may be detected as high-frequency residuals in spectral fits (see analysis in Section 3.1), they are very low-level ($\leq 2\%$, or $< 2\sigma$), so a correction is not applied.

2.2 JWST/NIRCam

We downloaded all available NIRCam images from the Mikulski Archive for Space Telescopes (MAST⁴): F115W, F150W, F200W,

³ Because the images were aligned by matching their brightest spaxels, the positional uncertainty is calculated by multiplying the cell sizes of each image ($0.05''$ for NIRSpec IFU and $0.063''$ for NIRCam) by 0.5, and adding them in quadrature.

⁴ <https://mast.stsci.edu/portal/Mashup/Clients/Mast/Portal.html>

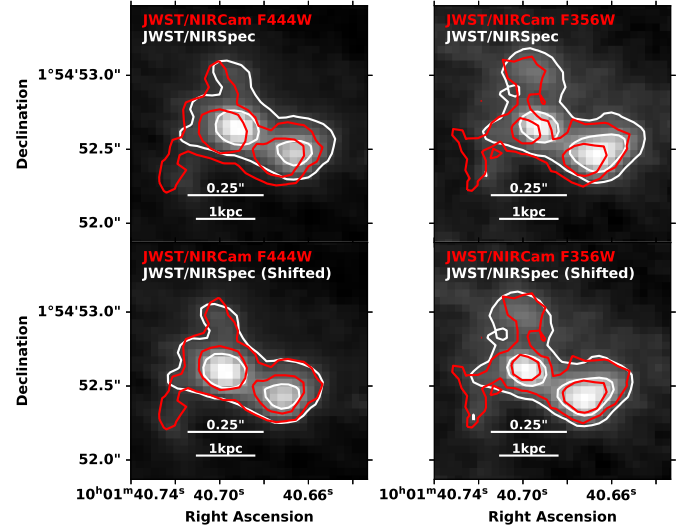


Figure 1. Comparison of JWST/NIRCam images and JWST/NIRSpec IFU data cube integrated over NIRCam filter bandpasses: F444W (left column) and F356W (right column). In each panel, the collapsed NIRSpec emission is depicted as the background greyscale and illustrative white contours, while the NIRCam data are shown as red contours. Angular and physical scales are shown in the lower left corner of each panel. The JWST emission in the top row is shown without the astrometric correction, while the lower row includes the alignment to the NIRCam data.

F277W, F356W, and F444W (Project 1840, PI J. Alvarez-Marquez). These data have been analysed in detail in Sugahara et al. (2024), and are well aligned with each other. By searching for significant emission in each image from stars in the *Gaia* DR3 catalogue (Gaia Collaboration et al. 2016, 2021), we find that they feature an absolute astrometric uncertainty of $< 0.2''$ (see Appendix B).

2.3 ALMA

Due to the bright nature of this high-redshift source, ALMA has been used to target its emission in CO(6-5), CO(7-6), and [CI](2-1) (2018.1.01673.S, PI Hashimoto), [C II]158 μm (2016.1.00954.S, PI Inoue), [O III]88 μm (2016.1.00954.S and 2017.1.00190.S, PI Inoue), and [N II]122 μm (2019.1.01491.S, PI Inoue). In order to compare the distribution of these lines (with their underlying continuum emission) and our data, we re-image each dataset.

To begin, we download all data from the ALMA data archive and run the calibration pipeline provided by NRAO staff⁵. The calibrated data for B14-65666 was split out, and a 30 s time average was performed to ease data usage. Data were combined for each band (3, Claude et al. 2008; Kerr et al. 2014; 6, Kerr et al. 2004; Ediss et al. 2004; 7, Mahieu et al. 2012; 8, Sekimoto et al. 2008).

Continuum images were created with the CASA task *tclean* in multi-frequency synthesis (MFS) mode, natural weighting, cell sizes of $1/5^{\text{th}}$ the FWHM of the minor axis of the synthesised beam, and excluding all data within $\pm 1000 \text{ km s}^{-1}$ of expected line emission. ‘Clean’ continuum maps were created by cleaning down to $3\times$ the RMS noise level of initial ‘dirty’ images.

No significant line emission is detected for CO(6-5), CO(7-6), [CI](2-1), or [N II]122 μm (as originally found by Hashimoto et al. 2023a and Sugahara et al. 2021), while [C II]158 μm and [O III]88 μm

⁵ 2019.1.01491.S was calibrated directly by the ALMA helpdesk.

Instrument	Name	λ_{obs} [μm]	λ_{rest} [μm]
JWST/NIRCam Imaging	F115W	1.154	0.142
JWST/NIRCam Imaging	F150W	1.501	0.184
JWST/NIRCam Imaging	F200W	1.990	0.244
JWST/NIRCam Imaging	F277W	2.786	0.342
JWST/NIRCam Imaging	F356W	3.563	0.437
JWST/NIRSpec IFU	4 μm	4.000	0.491
JWST/NIRCam Imaging	F444W	4.421	0.542
ALMA	Band8	740.228	90.803
ALMA	Band7	999.308	122.584
ALMA	Band6	1332.411	163.446
ALMA	Band3	3331.027	408.615

Table 2. List of continuum data. For each dataset, we list a representative wavelength in the observed and rest frame (assuming $z = 7.1520$): pivot wavelengths for each JWST imaging filter and average wavelengths for each ALMA band.

are strongly detected. For the latter two lines, we create clean line+continuum cubes using CASA *tclean* in ‘cube’ mode with natural weighting and cell sizes of $1/5^{\text{th}}$ the FWHM of the minor axis of the synthesised beam. Each cube is continuum subtracted in the image plane⁶ using the CASA task *imcontsub*. The continuum level in each spaxel is found by fitting the line-free channels in the spectrum with a first-order polynomial (using the same $\pm 1000 \text{ km s}^{-1}$ range as above), and the resulting continuum emission is removed. This results in a continuum-free data cube.

2.4 Multi-wavelength comparison

Due to the plethora of previous observations, we are able to compare the spatial distribution of continuum emission from $\lambda_{rest} = 1420 \text{ \AA}$ to $\sim 0.4 \text{ mm}$. The resulting maps (Figure 2) reveal emission in multiple regions. Detailed SED fitting was performed by Sugahara et al. (2024), so we focus here only on the distribution of emission.

All of the JWST/NIRCam images of Figure 2 were created using spectral filters that do not discriminate between continuum and line emission. However, the $\lambda_{obs} = 4 \mu\text{m}$ JWST/NIRSpec IFU map and each ALMA map exclude line emission. Note that together, F356W and F444W span the wavelength range of our NIRSpec data ($\lambda_{obs} \sim 3 - 5 \mu\text{m}$), and thus contain multiple strong emission lines (e.g., [OII] $\lambda\lambda 3726, 3729$ in F356W and [OIII] $\lambda\lambda 4959, 5007$ in F444W).

Each of the rest-UV and rest-optical continuum images with significant emission shows a similar compact distribution focused in the two core regions. The high-resolution NIRCam observations reveal that the east core region is compact, while the west emission has extensions to the northeast and northwest (i.e., forming a ‘V’-shape). While the band 8 continuum (near the peak of the dust SED; Sugahara et al. 2024) presents a similar picture, the band 6 continuum instead peaks at the intersection of the two cores (as seen in other works; Hashimoto et al. 2019; Sugahara et al. 2024; see discussion in Section 4.3). The ALMA band 3 image does not show emission, as this wavelength lies at the low-flux red end of the warm dust emission.

This clumpy morphology was recently noted by the JWST/NIRCam analysis of Sugahara et al. (2024), who define a circular ‘Total’ aperture that includes all flux ($r = 0.90''$) and two smaller circular apertures centred on the bright cores (‘E-core’ and

‘W-core’, $r = 0.22''$). The extended emission is measured using one elliptical aperture to the north of E-core (semi-minor axes of $0.35''$ and $0.20''$, with major axis aligned 90° counterclockwise from north) and another elliptical aperture to the southeast of E-core (semi-minor axes of $0.50''$ and $0.25''$, with major axis aligned 30° counterclockwise from north). Two larger ellipses are also included that cover the west half of the field (‘W’, including W-core) and the east half (‘E’, including E-core and most of the two tail regions).

Based on the rest-optical emission that we observe with JWST/NIRSpec, we adopt similar apertures that are adapted to cover separate areas of emission with no overlap (see lower right panel of Figure 2). These include a slightly larger aperture that covers the full field (‘Full’, $r = 1.0''$)⁷, the two core regions (‘Core-E’ and ‘Core-W’), adjusted versions of the two tail regions (‘Clump-N’ and ‘Arc-S’), and a new region that contains low-level line emission to the west of Core-W (‘Clump-W’). The locations and sizes of ‘Clump-W’, ‘Clump-N’, and ‘Arc-S’ are motivated by the presence of line emission (see Section 3.1).

3 NIRSPEC ANALYSIS

Our JWST/NIRSpec IFU data cube allows us to explore line and continuum emission from B14-65666 on a spatially and spectrally resolved basis. In this Section, we first characterise each region by fitting their integrated spectra (Section 3.1). We then exercise the power of the NIRSpec IFU by extracting and fitting spectra from each individual spaxel (Section 3.2), opening a more detailed view into the ISM conditions and morpho-kinematics of B14-65666.

3.1 Spatially integrated spectral analysis

First, we characterise the emission in the field by extracting integrated spectra from our NIRSpec data cube using the apertures of Figure 2. The spectra are presented in Figure 3. From this initial comparison of each spectrum, it is clear that each region contains multiple significant line detections, with some lines being asymmetric, and there is a range of brightnesses across the field. To characterise each region further, we fit each spectrum with a combined line and continuum model.

3.1.1 Model description

For the spectrum from each aperture, we assume that the continuum is described by a single power law model. Since the bluest edge of our data ($\lambda_{rest} \sim 3620 \text{ \AA}$) extends slightly bluewards of the Balmer break ($\lambda_{rest} \sim 3646 \text{ \AA}$), it is possible that the continuum is affected by Balmer absorption features and/or in a change in slope bluewards of [NeIII] $\lambda 3869$, as seen in quenched galaxies (e.g., D’Eugenio et al. 2024a; Looser et al. 2024). However, we do not detect such features in our data, and the simple model returns low residuals (see Figure C1).

To account for line emission, we include [OII] $\lambda\lambda 3726, 3729$, [NeIII] $\lambda\lambda 3869, 3968$, Balmer lines (H ζ , H δ , H ϵ , H β), [OIII] $\lambda\lambda 3633$, and [OIII] $\lambda\lambda 4959, 5007$ in our model. Because some lines exhibit asymmetric wings in multiple spaxels, we follow other investigations of high- z galaxies with NIRSpec and fit each emission line with two

⁶ Due to the resolved, relatively weak nature of the line emission, this is preferable to visibility-space continuum subtraction.

⁷ We choose a slightly larger total aperture than Sugahara et al. (2024) to capture extended [OIII] $\lambda 5007$ emission.

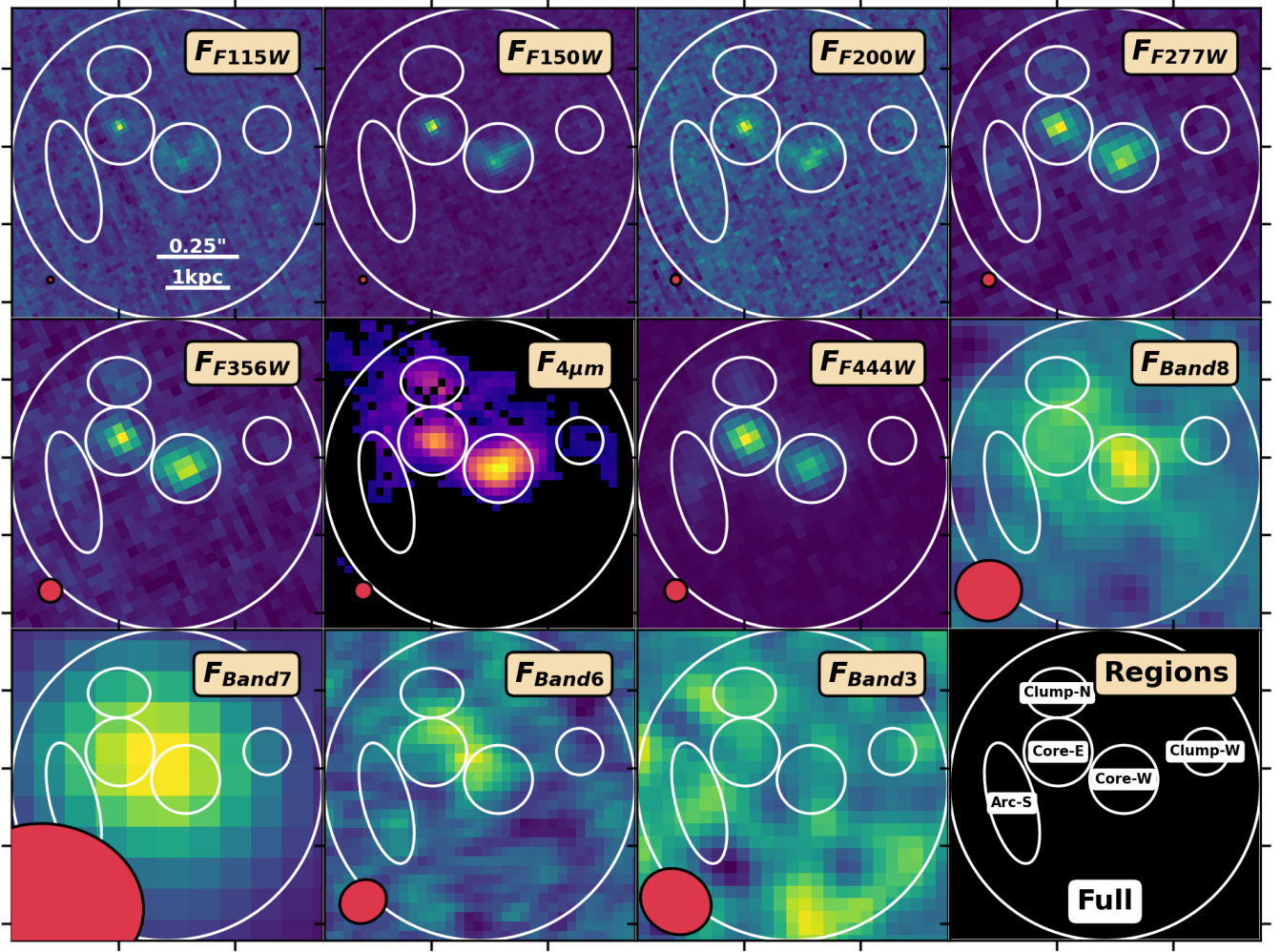


Figure 2. Gallery of multi-wavelength continuum data (see Table 2 for details) in order of increasing λ_{obs} . Each panel displays a field of view of $2'' \times 2''$ ($\sim 10.3 \times 10.3 \text{ kpc}^2$), centred on $10\text{h}01\text{m}40.68\text{s} + 1^\circ 54' 52.39''$. An angular and physical scale is shown in the first panel. For each, we show the PSF as a red ellipse to the lower left. North is up and east is to the left. The final panel details our six regions of study: the two dominant cores, two smaller clumps, one arc, and a large circular aperture that encompasses all emission. The JWST/NIRSpec continuum map ($\lambda_{obs} = 4 \mu\text{m}$), which was derived through spaxel-by-spaxel fit (see Section 3.2 for details), is displayed in a different colourmap for emphasis.

components: one narrow ($\text{FWHM} \leq 350 \text{ km s}^{-1}$) and one broad, representing tidal features or an outflow ($350 \leq \text{FWHM} \leq 1000 \text{ km s}^{-1}$; e.g., Lamperti et al. 2024; Rodríguez Del Pino et al. 2024). A one-Gaussian fit returns large residuals for each of the strong lines ([OIII] $\lambda 5007$, [OIII] $\lambda 4959$, [OII] $\lambda \lambda 3726, 3729$), suggesting that a two-Gaussian fit is needed. This approach is preferred to Voigt profiles (e.g., Jones et al. 2024b), as it allows for the fitting of asymmetric lines. The LSF-corrected FWHM and redshift of all lines are fixed for each component.

To lower the degrees of freedom in our model, we make the standard assumption of case B recombination (Baker & Menzel 1938; e.g., Hu et al. 2024; Solimano et al. 2024; Venturi et al. 2024)⁸ and use the python package PYNEB (Luridiana et al. 2015) to calculate line ratios based on ISM conditions (i.e., electron temperature T_e and density n_e ; see further discussion in Appendix E). The ratios of [NeIII] $\lambda 3968$ /[NeIII] $\lambda 3869$ and [OIII] $\lambda 5007$ /[OIII] $\lambda 4959$

are fixed by atomic physics (0.301 and 2.984, respectively). To derive each of the other line ratios ($\text{H}\gamma/\text{H}\beta$, $\text{H}\delta/\text{H}\beta$, $\text{H}\epsilon/\text{H}\beta$, $\text{H}\zeta/\text{H}\beta$, [OII] $\lambda 3726$ /[OII] $\lambda 3729$, [OIII] $\lambda 4363$ /[OIII] $\lambda 5007$), we adopt a fiducial density of $n_e = 200 \text{ cm}^{-3}$ (Sugahara et al. 2024) and allow T_e to range from $(0.5 - 3.0) \times 10^4 \text{ K}$. If the model returns poor constraints on T_e , then we assume a fiducial value of $1.2 \times 10^4 \text{ K}$ (Sugahara et al. 2024).

While the ratio of the two lines in the [OII] $\lambda \lambda 3726, 3729$ doublet is a useful tracer of electron density (e.g., Kewley et al. 2019), their close separation requires high spectral resolution for detailed fitting ($R \gtrsim 2700$; Comparat et al. 2013). This is achievable with high-resolution JWST/NIRSpec gratings (e.g., Rodríguez Del Pino et al. 2024; Chisholm et al. 2024), but our resolution is a factor of ~ 3 more coarse. Therefore, we fix n_e to the fiducial value and calculate the ratio of [OII] $\lambda 3726$ /[OII] $\lambda 3729$ using PYNEB.

Our model should also take into account the effect of dust reddening. To do this, we additionally model the B-V colour excess $E(B-V)$, which may be used to convert an observed line flux (F_{obs}) to its

⁸ Although we note that the applicability of this assumption for high-redshift galaxies has recently been called into question (Scarlata et al. 2024).

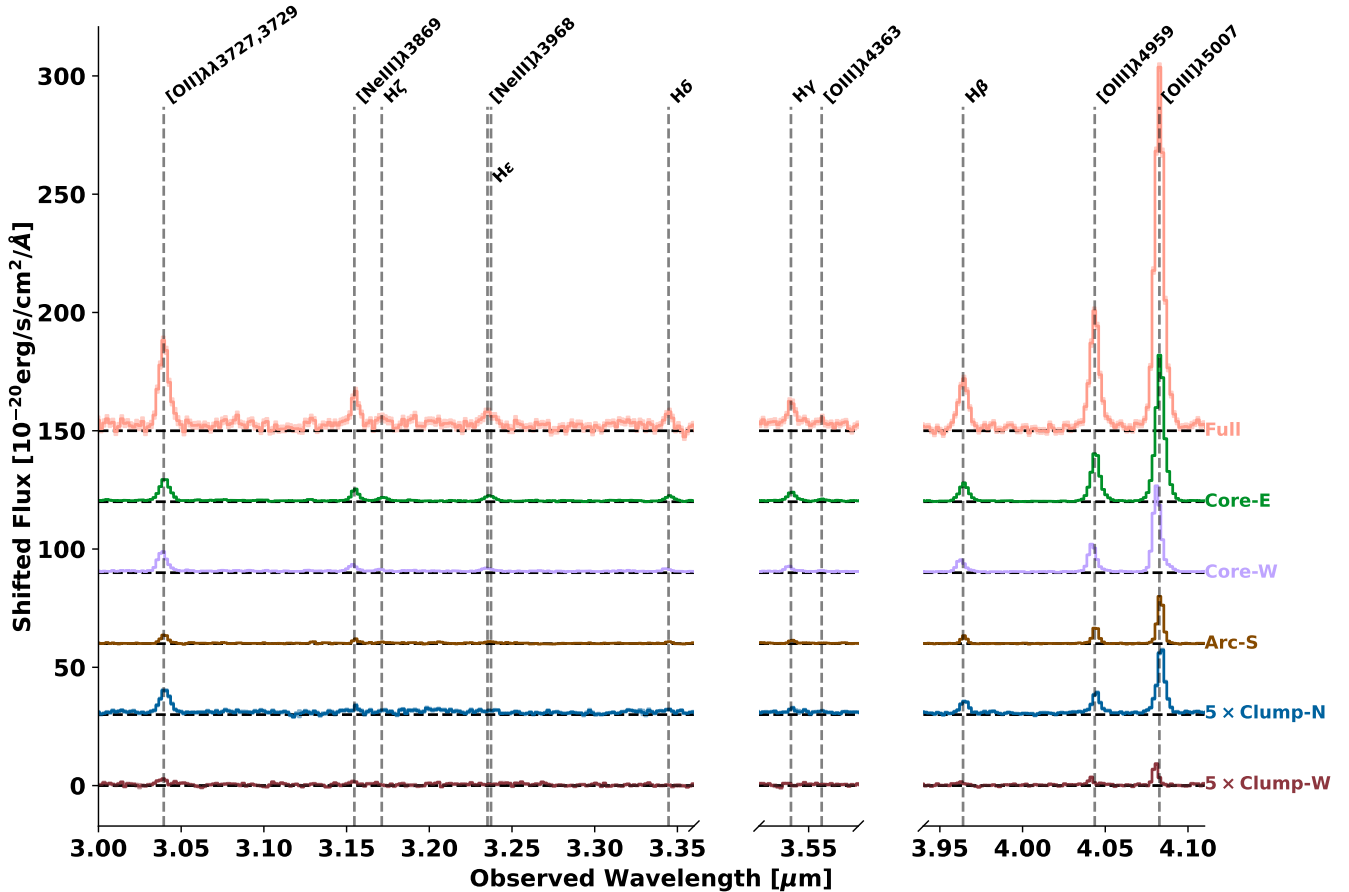


Figure 3. Spectra extracted from each region from Figure 2, shifted vertically for clarity. Clump-N and Clump-N features weaker emission, so we multiply these spectra by a factor of 5 to ease comparison. Dashed vertical lines denote the wavelengths of detected lines, assuming $z = 7.1520$. A more detailed view of each line is shown in Figure C1.

dust-extincted value:

$$F_{int} = F_{obs} 10^{k(\lambda)E(B-V)/2.5} \quad (1)$$

where $k(\lambda)$ is the assumed dust attenuation curve (Calzetti et al. 2000). The work of Sugahara et al. (2024) estimated the dust reddening of the stellar continuum in this system to be $A_V^* \sim 0.3 - 1.2$, which corresponds to ionised gas colour excess of $E(B - V) \sim 0.2 - 0.7$ (assuming Calzetti et al. 2000 attenuation law). Leaving $E(B - V)$ as a free parameter results in poor fits, but a simple exploration (see Appendix E3) reveals that a lower colour excess ($\sim 0.0 - 0.2$) is preferred by our model. Thus, we assume $E(B - V) = 0.2$ throughout.

Our fits take the fiducial line spread function (LSF) of NIR-Spec⁹ into account. This varies from $\sim 400 \text{ km s}^{-1}$ (FWHM) at the wavelength of [OII] $\lambda\lambda 3726, 3729$ to $\sim 300 \text{ km s}^{-1}$ at the wavelength of [OIII] $\lambda 5007$. We experimented with allowing the LSF to vary from the fiducial value by 50%, but the resulting fits were not well-constrained. When fitting the intrinsic FWHM of the narrow component, we are not able to constrain the intrinsic width of very narrow lines (e.g., $< 50 \text{ km s}^{-1}$). When the fitting routine returns a narrow intrinsic width, we fix the intrinsic width to 0, and state that the line is unresolved (see Table 3).

⁹ As recorded in the JWST documentation; <https://jwst-docs.stsci.edu/jwst-near-infrared-spectrograph/nirspec-instrumentation/nirspec-dispersers-and-filters>

For each spectrum, our model therefore has three contributions: the power-law continuum (with a variable slope and normalisation) and the broad and narrow line-emitting components (each with its variable T_e , z , $FWHM$, and dust-corrected fluxes of all independent lines: [OII] $\lambda\lambda 3726$, [NeIII] $\lambda 3869$, H β , [OIII] $\lambda 5007$). We fix n_e and $E(B - V)$ to be constant for all models, and use PYNEB to estimate the dust-corrected fluxes of each of the other lines (i.e., [OII] $\lambda 3729$, H γ , [NeIII] $\lambda 3968$, He, H δ , H γ , [OIII] $\lambda 4363$, and [OIII] $\lambda 4959$). Using LMFIT (Newville et al. 2014), we fit this combined model to each spectrum. An initial fit is performed where all variables are allowed to vary. The results of this fit are inspected, and lines with poorly determined (i.e., $< 3\sigma$) or negligible fluxes (i.e., $< 10^{-21} \text{ erg s}^{-1} \text{ cm}^{-2}$) are removed from the model before the fit is repeated. This process repeats until LMFIT reports convergence. The best-fit continuum and line properties are presented in Table 3 while the resulting spectra are shown in Figure C1.

3.1.2 Results and further measurables

Each spectrum features strong [OII] $\lambda\lambda 3726, 3729$, H β , and [OIII] $\lambda\lambda 4959, 5007$ emission, while [NeIII] $\lambda 3869$ is detected from most regions (see Table 3). All regions have T_e values within 1σ of the fiducial value of $1.2 \times 10^4 \text{ K}$, comparable to conditions in other high-redshift galaxies (e.g., Hsiao et al. 2024a; Hu et al. 2024; Torralba-Torregrosa et al. 2024).

Table 3. Best-fit continuum and line properties of each component, as derived through spectral fits. The best-fit continuum flux density at $\lambda_{obs} = 4\mu\text{m}$ is given in units of $[10^{-20}\text{erg s}^{-1}\text{cm}^{-2}\text{\AA}^{-1}]$. The best-fit dust-corrected fluxes of each line are given in units of $[10^{-20}\text{erg s}^{-1}\text{cm}^{-2}]$. For the narrow and broad component, we list the FWHM (in units of $[\text{km s}^{-1}]$) and redshift. Entries of ‘Unres.’ indicate that the narrow emission was best-fit with a line width equal to the LSF.

		Full	Core-W	Core-E	Clump-W	Arc-S	Clump-N
$F_{\lambda}(\lambda_{obs} = 4\mu\text{m})$		1.139 ± 0.072	0.375 ± 0.008	0.242 ± 0.008	0.032 ± 0.004	0.052 ± 0.007	0.141 ± 0.006
Continuum Slope		-3.29 ± 0.33	-2.48 ± 0.11	-2.89 ± 0.18	-3.86 ± 0.63	-4.70 ± 0.64	-1.70 ± 0.23
$FWHM$	N	280 ± 19	227 ± 6	144 ± 11	Unres.	Unres.	Unres.
	B	760 ± 65	755 ± 23	653 ± 10	-	669 ± 84	557 ± 29
z	N	7.1517 ± 0.0001	7.1486 ± 0.0001	7.1528 ± 0.0001	7.1475 ± 0.0002	7.1532 ± 0.0001	7.1541 ± 0.0001
	B	7.1527 ± 0.0004	7.1547 ± 0.0005	7.1532 ± 0.0001	-	7.1524 ± 0.0007	7.1537 ± 0.0002
$F_{[\text{OII}]\lambda\lambda 3727, 3729}$	N	4047 ± 730	1179 ± 44	507 ± 73	77 ± 10	556 ± 20	-
	B	3540 ± 837	487 ± 50	1519 ± 88	-	-	423 ± 16
	Total	7588 ± 1111	1666 ± 67	2026 ± 114	77 ± 10	556 ± 20	423 ± 16
$F_{[\text{NeIII}]\lambda 3689}$	N	2116 ± 156	339 ± 24	466 ± 42	30 ± 10	207 ± 15	-
	B	-	125 ± 32	306 ± 55	-	-	-
	Total	2116 ± 156	464 ± 40	772 ± 69	30 ± 10	207 ± 15	-
$F_{\text{H}\beta}$	N	1996 ± 313	553 ± 20	489 ± 30	27 ± 5	328 ± 10	64 ± 13
	B	1771 ± 373	235 ± 25	804 ± 37	-	-	84 ± 19
	Total	3767 ± 487	789 ± 32	1294 ± 48	27 ± 5	328 ± 10	148 ± 23
$F_{[\text{OIII}]\lambda 5007}$	N	15609 ± 1408	3972 ± 74	4197 ± 142	175 ± 6	1879 ± 33	341 ± 22
	B	8915 ± 1364	1204 ± 78	5546 ± 139	-	331 ± 33	434 ± 24
	Total	24524 ± 1961	5176 ± 107	9743 ± 199	175 ± 6	2210 ± 47	775 ± 32

We use the best-fit line fluxes to calculate standard line ratios:

- $\text{O32} \equiv [\text{OIII}]\lambda 5007 / ([\text{OII}]\lambda\lambda 3726, 3729)$
- $\text{R3} \equiv [\text{OIII}]\lambda 5007 / \text{H}\beta$
- $\text{R2} \equiv [\text{OII}]\lambda\lambda 3726, 3729 / \text{H}\beta$
- $\text{R23} \equiv ([\text{OIII}]\lambda\lambda 4959, 5007 + [\text{OII}]\lambda\lambda 3726, 3729) / \text{H}\beta$
- $\text{Ne3O2} \equiv [\text{NeIII}]\lambda 3869 / ([\text{OII}]\lambda\lambda 3726, 3729)$

All of these (with the exception of Ne3O2) are then used to calculate the gas-phase metallicity using the strong-line diagnostics calibrated by Curti et al. (2020). The resulting values are listed in Table 4. We find total gas-phase metallicities of $(Z_g/Z_{\odot}) \sim 0.24 - 0.39$ for each region, which are slightly lower for the narrow components than for the broad. This is in general agreement with the values derived by Sugahara et al. (2024) using optical-FIR diagnostics (i.e., $Z_g/Z_{\odot} \approx 0.2$). The SED-based stellar metallicity of Sugahara et al. (2024) ($Z_*/Z_{\odot} = 0.21 \pm 0.05$) is lower than our total gas-phase metallicity ($Z_g/Z_{\odot} = 0.29 \pm 0.05$), as seen in other $z > 6$ galaxies (e.g., Scholtz et al. 2024; Marconcini et al. 2024a).

Next, we infer the star formation rate (SFR) using the best-fit dust-corrected $\text{H}\beta$ flux. Using PYNEB, we estimate the extinction-free ratio of $\text{H}\alpha/\text{H}\beta = 2.828$ (see Appendix E). Combining this with the calibration of Kennicutt (1998) yields:

$$\frac{\text{SFR}_{\text{H}\alpha}}{[\text{M}_{\odot} \text{yr}^{-1}]} = \frac{C_{\text{SFR}} \times 2.828 \times I_{\text{H}\beta}}{[\text{erg s}^{-1} \text{cm}^{-2}]} \left(\frac{4\pi D_L}{[\text{cm}]} \right)^2 \frac{[\text{erg s}^{-1} \text{M}_{\odot}^{-1} \text{yr}]}{1.26 \times 10^{41}} \quad (2)$$

where the factor of C_{SFR} is included to convert from a Salpeter (1955) IMF to a Chabrier (2003) IMF. Previous works used a range of $C_{\text{SFR}} \sim 0.56 - 0.65$ (e.g., Panter et al. 2007; Longhetti & Saracco 2009; Dutton et al. 2010; González et al. 2010; Béthermin et al. 2012; Driver et al. 2013; Madau & Dickinson 2014; Caputi et al. 2017; Figueira et al. 2022; Hsiao et al. 2024b). We briefly note that some recent investigations of high redshift galaxies ($z > 6$) with JWST have

instead used conversion factors based on stellar population synthesis models (Reddy et al. 2018, 2022). These models, which assume a low metallicity, result in lower factors (e.g., $C_{\text{SFR}} = 0.27$; Saxena et al. 2023; Curti et al. 2024, $C_{\text{SFR}} \sim 0.40$; Hsiao et al. 2024a). In this work, we will adopt a Chabrier (2003) IMF and $C_{\text{SFR}} \sim 0.61$, as in another high-redshift JWST work (Hsiao et al. 2024b).

The Full aperture yields a total SFR = $308 \pm 39 \text{M}_{\odot} \text{yr}^{-1}$, which is in agreement (i.e., $< 2\sigma$ discrepant) with the SED-based estimate of Hashimoto et al. (2019, SFR = $200^{+82}_{-38} \text{M}_{\odot} \text{yr}^{-1}$) as well as the instantaneous (SFR₀ = $225^{+71}_{-56} \text{M}_{\odot} \text{yr}^{-1}$) and 10 Myr-averaged (SFR_{10Myr} = $207^{+65}_{-51} \text{M}_{\odot} \text{yr}^{-1}$) values from Sugahara et al. (2024). Since SFR_{H α} traces star formation over the past 5 Myr (e.g., Flores Velázquez et al. 2021; Tacchella et al. 2022), this agreement is expected.

The O32 ratio has been shown to be an excellent tracer of the ionisation parameter U (e.g., Nagao et al. 2006; Papovich et al. 2022). Following other recent works (e.g., Witstok et al. 2021; Boyett et al. 2024; Zamora et al. 2024), we convert the derived O32 values to U using the relation of Díaz et al. (2000):

$$\log_{10}(U) = 0.80 \log_{10}(\text{O32}) - 3.02 \quad (3)$$

which was derived using single star ionisation models. This yields values of $-2.7 \lesssim \log_{10} U \lesssim -2.3$ for most regions, with slightly lower values for Clump-N. Thus, the regions of B14-65666 show similar ionisation parameters as galaxies in the $2.7 < z < 6.3$ sample of Reddy et al. (2023) and the lower redshift ($1.1 < z < 2.3$) sample of Papovich et al. (2022).

3.2 Spaxel-by-spaxel fits

We can exploit the power of the NIRSpect IFU to extract physical properties on a spatially resolved basis by fitting combined line and continuum models to the spectra of each spaxel. This is enhanced

Table 4. Best-fit line ratios, gas-phase metallicities (Curti et al. 2020), electron temperatures, H β -based SFRs, and ionisation parameter U (see Section 3.1.2) of each region. Temperatures in parentheses are assumed.

		Full	Core-W	Core-E	Clump-W	Arc-S	Clump-N
O32	N	3.86 ± 0.78	3.37 ± 0.14	8.29 ± 1.23	2.28 ± 0.31	3.38 ± 0.13	-
	B	2.52 ± 0.71	2.47 ± 0.30	3.65 ± 0.23	-	-	1.02 ± 0.07
	Total	3.23 ± 0.54	3.11 ± 0.14	4.81 ± 0.29	2.28 ± 0.31	3.97 ± 0.16	1.83 ± 0.10
R3	N	7.82 ± 1.42	7.18 ± 0.29	8.58 ± 0.60	6.48 ± 1.24	5.73 ± 0.20	5.31 ± 1.15
	B	5.03 ± 1.31	5.12 ± 0.64	6.89 ± 0.36	-	-	5.16 ± 1.18
	Total	6.51 ± 0.99	6.56 ± 0.30	7.53 ± 0.32	6.48 ± 1.24	6.74 ± 0.25	5.22 ± 0.84
R2	N	2.03 ± 0.48	2.13 ± 0.11	1.04 ± 0.16	2.84 ± 0.65	1.70 ± 0.08	-
	B	2.00 ± 0.63	2.07 ± 0.31	1.89 ± 0.14	-	-	5.03 ± 1.14
	Total	2.01 ± 0.39	2.11 ± 0.12	1.57 ± 0.11	2.84 ± 0.65	1.70 ± 0.08	2.85 ± 0.45
R23	N	12.47 ± 2.20	11.71 ± 0.47	12.48 ± 0.87	11.49 ± 2.21	9.35 ± 0.32	-
	B	8.72 ± 2.16	8.90 ± 1.08	11.09 ± 0.57	-	-	11.92 ± 2.69
	Total	10.71 ± 1.58	10.88 ± 0.49	11.62 ± 0.48	11.49 ± 2.21	10.70 ± 0.39	9.83 ± 1.55
Ne3O2	N	0.52 ± 0.10	0.29 ± 0.02	0.92 ± 0.16	0.39 ± 0.14	0.37 ± 0.03	-
	B	-	0.26 ± 0.07	0.20 ± 0.04	-	-	-
	Total	0.28 ± 0.05	0.28 ± 0.03	0.38 ± 0.04	0.39 ± 0.14	0.37 ± 0.03	-
Z [Z_{\odot}]	N	0.27 ± 0.04	0.29 ± 0.04	0.18 ± 0.03	0.35 ± 0.05	0.29 ± 0.04	-
	B	0.34 ± 0.06	0.34 ± 0.05	0.28 ± 0.04	-	-	0.47 ± 0.07
	Total	0.29 ± 0.05	0.30 ± 0.04	0.24 ± 0.03	0.35 ± 0.05	0.26 ± 0.04	0.39 ± 0.05
T_e [10^4 K]	N	(1.2)	1.02 ± 0.21	1.39 ± 0.24	(1.2)	(1.2)	(1.2)
	B	(1.2)	1.93 ± 0.77	1.09 ± 0.30	(1.2)	(1.2)	(1.2)
$SFR_{H\beta}$ [$M_{\odot} yr^{-1}$]	N	163 ± 25	45 ± 1	39 ± 2	2 ± 1	26 ± 1	5 ± 1
	B	145 ± 30	18 ± 2	66 ± 3	-	-	6 ± 1
	Total	308 ± 39	64 ± 2	106 ± 3	2 ± 1	26 ± 1	12 ± 1
$\log_{10}(U)$	N	-2.55 ± 0.07	-2.60 ± 0.01	-2.29 ± 0.05	-2.73 ± 0.05	-2.60 ± 0.01	-
	B	-2.70 ± 0.10	-2.71 ± 0.04	-2.57 ± 0.02	-	-	-3.01 ± 0.02
	Total	-2.61 ± 0.06	-2.63 ± 0.02	-2.47 ± 0.02	-2.73 ± 0.05	-2.54 ± 0.01	-2.81 ± 0.02

through direct comparison to morpho-kinematic maps of ALMA data, which we create in an identical fashion.

3.2.1 NIRSpec IFU map creation

To analyse our NIRSpec IFU data, we adopt a model and fitting procedure nearly identical to that of Section 3.1. Due to the lower S/N per spaxel, we adopt a constant fiducial $T_e = 1.2 \times 10^4$ K (Sugahara et al. 2024). The resulting total intensity maps are included in Figure 4, while the intensity maps of the narrow and broad components are presented in Figure D1. The best-fit continuum ($\lambda_{obs} = 4 \mu\text{m}$) map from this analysis was included in the continuum gallery of Figure 2. Note that because of our model assumptions, the corresponding map of [NeIII] $\lambda 3968$ is identical to that of [NeIII] $\lambda 3869$, but with a constant scaling factor (see Appendix E). Similarly, each of the other Balmer lines (H γ , H δ , H ϵ , H ζ) can be found from the H β distribution, and [OIII] $\lambda 4959$ and [OIII] $\lambda 4363$ can be found from the [OIII] $\lambda 5007$ distribution.

Our fits also allow us to explore the kinematics of the field by extracting parameters from each spaxel. This is done by considering the best-fit [OIII] $\lambda 5007$ model, converting it to a cumulative distribution function (CDF), and calculating multiple non-parametric v_N values (i.e., velocities at which the CDF reaches $N\%$). In each case we assume a fiducial zero-velocity redshift of $z = 7.1520$. Figure 5 shows v_{50} (the mean velocity) and the asymmetry ($|v_{50} - v_{10}| - |v_{50} - v_{90}|$), while Figure 6 shows $w_{80} \equiv v_{90} - v_{10}$ (a measure of linewidth).

3.2.2 ALMA map creation

Previous analyses of the ALMA data for this source created moment maps (Hashimoto et al. 2019, 2023a; Sugahara et al. 2021, 2024), which are non-parametric measures of the total intensity (moment 0), intensity-weighted mean velocity (moment 1), and velocity dispersion (moment 2)¹⁰. Here, we instead use Gaussian spectral models to fit the ALMA data on a spaxel-by-spaxel basis, resulting in morpho-kinematic maps that may be directly compared to our NIRSpec maps.

Because each ALMA data cube only contains a single line ([C II] $\lambda 158 \mu\text{m}$ or [O III] $\lambda 88 \mu\text{m}$), the fitting process is much simpler than that of Section 3.1 or 3.2. First, we construct an error spectrum for each continuum-subtracted data cube by taking the RMS noise level of each spectral channel. Considering the possibility that each line may be fit by two Gaussian components (i.e., narrow and broad), the spectrum extracted from each spaxel is fit with these two Gaussians and an underlying first-order polynomial continuum using LMFIT. However, this approach only reveals a few spaxels where a two-Gaussian model returns a better fit (i.e., a lower reduced χ^2) in either cube. Because these potential areas are smaller than a synthesised beam and are not aligned with the broad emission found in [OIII] $\lambda 4959, 5007$ emission, they are likely artifacts (e.g., incomplete continuum subtraction, data combination, imaging). Thus, we

¹⁰ See CASA toolkit manual for more details: https://www.aoc.nrao.edu/~kgolap/casa_trunk_docs/CasaRef/image.moments.html

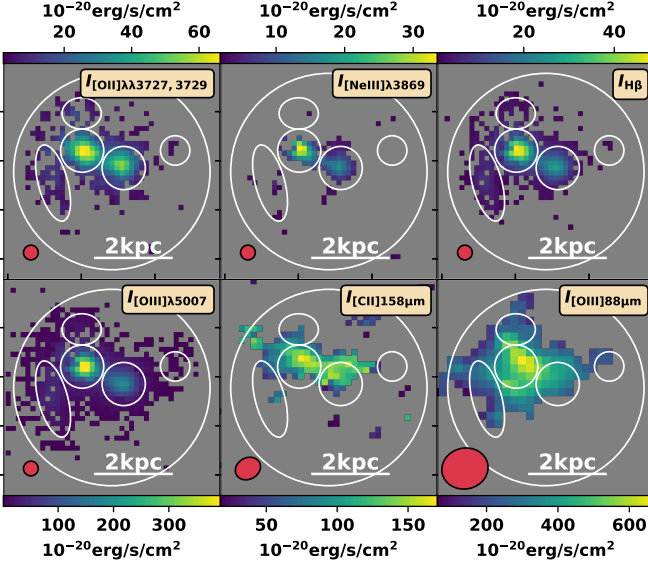


Figure 4. Integrated total fluxes of emission lines, as derived through spaxel-by-spaxel fit. Only $> 3\sigma$ fluxes are shown. Each panel displays a field of view of $2'' \times 2''$ centred on $10\text{h}01\text{m}40.68\text{s} + 1^\circ 54' 52.39''$. A physical scale bar of 2 kpc scale bar is included to the lower right in each panel. Similar plots for the narrow and broad components of the optical lines can be found in Figure D1.

adopt a single-Gaussian model. The resulting total intensity, v_{50} , and w_{80} maps are included in Figures 4, 5, and 6, respectively.

3.2.3 Distribution of emission

All of the rest-optical lines feature similar morphologies, with emission focused in the cores, a brighter Core-E, and diffuse emission that envelopes the two clumps and the arc. The rest-FIR lines are qualitatively similar, but they do not feature peaks in Core-W. The ALMA and JWST lines are further compared in Section 4.2.

When the JWST-detected lines are decomposed into narrow and broad components (Figure D1), a different flux distribution is observed. The narrow components of [OIII] $\lambda 5007$ and H β show nearly equal contributions from the two cores, while their broad emission is focused in Core-E with a weak tail to the southwest. The [NeIII] $\lambda 3968$ morphology is also similar, but with negligible broad emission. The [OII] $\lambda 3726, 3729$ morphology is unique in that the narrow component is strongly focused in Core-W, while the broad component is in Core-E.

3.2.4 Field kinematics

We find that [OIII] $\lambda 5007$, [C II] $158\mu\text{m}$, and [O III] $88\mu\text{m}$ feature similar distributions of v_{50} (Figure 5), with a strong east-west velocity gradient. There are slight differences between the maps, which may be ascribed to differences in sensitivity and resolution (e.g., beam smearing, spatial binning). As seen in other works (e.g., Telikova et al. 2024), [C II] $158\mu\text{m}$ and [O III] $88\mu\text{m}$ show similar line-of-sight velocity maps. Our v_{50} maps of the ALMA-detected lines are qualitatively similar to the moment 1 maps created by Hashimoto et al. (2019), but differ slightly due to differences in imaging (e.g., spaxel size) and velocity measurement method (i.e., Gaussian fit vs. moment 1). While such a symmetric velocity field could be interpreted as a signature of rotation, the disparate properties of each core (see

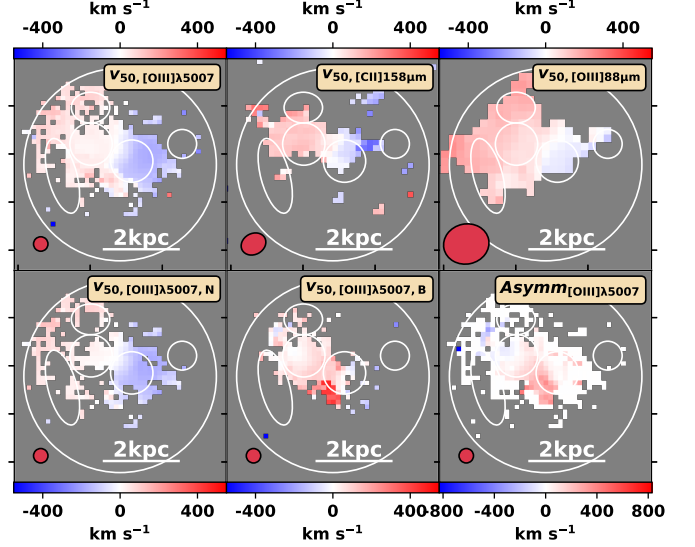


Figure 5. Line of sight velocity maps, as derived through spaxel-by-spaxel fits. The top row includes maps of v_{50} (i.e., the velocity at which each line reaches 50% of its total flux) for [OIII] $\lambda 5007$, [C II] $158\mu\text{m}$, and [O III] $88\mu\text{m}$. Maps of v_{50} for the narrow and broad component of [OIII] $\lambda 5007$ are shown in the first two panels of the lower row. The bottom right panel presents the best-fit asymmetry of [OIII] $\lambda 5007$ (see Section 3.2.1 for definition). Each panel displays a field of view of $2'' \times 2''$ centred on $10\text{h}01\text{m}40.68\text{s} + 1^\circ 54' 52.39''$. A physical scale bar of 2 kpc scale bar is included to the lower right in each panel. For each, we show the PSF as a red ellipse to the lower left. North is up and east is to the left.

Table 4, Figure 7) suggest a major merger instead (see Section 4.5 for further discussion).

The asymmetry map is mostly ~ 0 , reflecting the fact that the brighter narrow component is the primary emission for most spaxels. However, there is a region of positive asymmetry to the southeast of Core-W that indicates a more powerful red broad component. Indeed, the channel maps of both [OIII] $\lambda 4959$ and [OIII] $\lambda 5007$ contain low-level redshifted emission in this area, which may indicate a tidal feature or outflow.

We are also able to calculate w_{80} for each line (Figure 6). It is clear that Core-E has a higher w_{80} than Core-W, which is primarily caused by the stronger broad component in Core-E. The w_{80} map of [O III] $88\mu\text{m}$ shows a region with elevated velocity dispersion south of Core-E which slightly overlaps with the broad [OIII] $\lambda 5007$ emission, but the two cores show similar $w_{80, [\text{O III}]88\mu\text{m}}$. The two ALMA w_{80} maps are more similar to that of the narrow component of [OIII] $\lambda 5007$, suggesting that the gas emitting broad [OIII] $\lambda 5007$ is not detected in [C II] $158\mu\text{m}$ or [O III] $88\mu\text{m}$.

3.2.5 Gas metallicity, SFR, and ionisation

The best-fit line maps are used to create maps of gas-phase metallicity, SFR, and U (see Section 3.1 for ratio definitions and diagnostic information). The resulting maps for the combined best-fit models are shown in Figure 7, while the separate narrow and broad fits are shown in Figure D1.

The metallicity map of the narrow component reveals that Core-W has a value of ~ 0.3 solar, as shown in Section 3.1.2. Both cores show similar metallicities ($\sim 0.2 - 0.4$ solar). The broad component (which extends from Core-E to the southwest) shows a metallicity gradient, but due to the low S/N of the lines in this region, this is

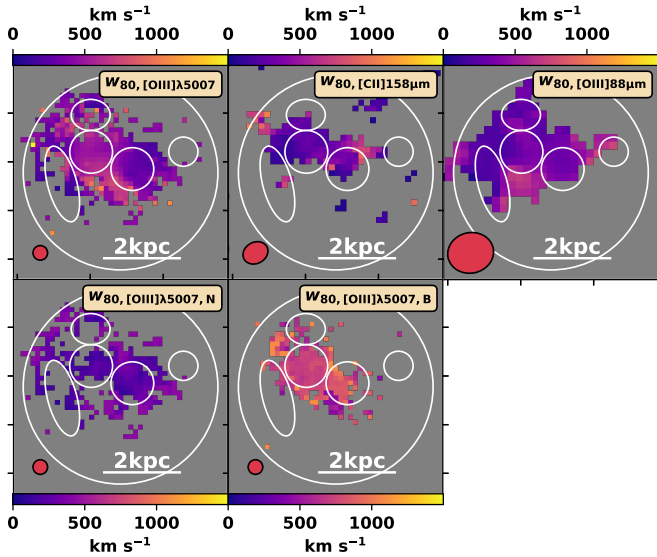


Figure 6. Maps of w_{80} (i.e., the difference in velocity between the points at which each line reaches 10% and 90% of its total flux), as derived through spaxel-by-spaxel fits for [OIII] λ 5007, [C II]158 μ m, and [O III]88 μ m. Maps of w_{80} for the narrow and broad component of [OIII] λ 5007 are shown in the lower row. Each panel displays a field of view of $2'' \times 2''$ centred on 10h01m40.68s +1 $^{\circ}$ 54'52.39". A physical scale bar of 2 kpc scale bar is included to the lower right in each panel. For each, we show the PSF as a red ellipse to the lower left. North is up and east is to the left.

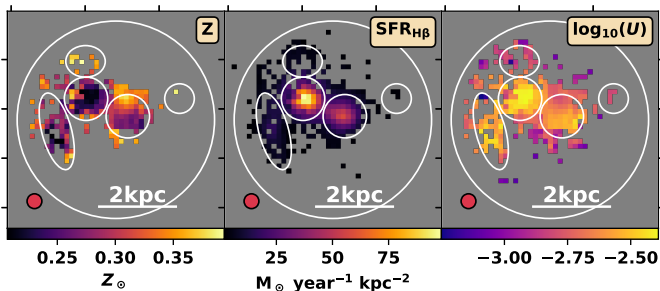


Figure 7. Line ratio diagnostics, as derived through spaxel-by-spaxel fit. Each panel displays a field of view of $2'' \times 2''$ centred on 10h01m40.68s +1 $^{\circ}$ 54'52.39". A physical scale bar of 2 kpc scale bar is included to the lower right in each panel. For each, we show the PSF as a red ellipse to the lower left. North is up and east is to the left.

tentative. However, while both the narrow and broad components show significant SFR (as traced by H β) in both cores, the broad component is isolated to Core-W. Core-E shows a higher U than Core-W.

4 DISCUSSION

4.1 Line ratio diagrams

Due to the wavelength coverage of our data, we do not have access to [NII] λ 6548,6584 or [SII] λ 6716,6731, and cannot utilise the standard [NII]-BPT or [SII]-VO87 diagrams (Baldwin et al. 1981; Veilleux & Osterbrock 1987) to search for evidence of AGN excitation. But the wealth of detected emission lines (see Table 3) allows us

to explore the nature of this field using other diagnostics: O32-R23, R3-R2, and Ne3O2 (see definitions in Section 3.1).

The ratios of each spatial region are shown in Figure 8. For comparison we also show the locations of low-redshift galaxies from SDSS (MPA-JHU DR8 catalogue; Kauffmann et al. 2003; Brinchmann et al. 2004), $5.5 \lesssim z \lesssim 9.5$ galaxies from the JADES survey (Cameron et al. 2023), $4.6 \lesssim z \lesssim 7.9$ galaxies from Mascia et al. (2023), $6.9 \lesssim z \lesssim 9.0$ galaxies from the CEERS survey (Tang et al. 2023), A2744- YD4 ($z = 7.88$; Witten et al. 2024), and the $5 \lesssim z \lesssim 9$ stacks created by Roberts-Borsani et al. (2024). Each of the line ratios from high-redshift galaxies has either been corrected for dust attenuation or has been measured for galaxies with no significant attenuation. Generally, we find that the different components of B14-65666 lie within the scatter of the JWST-observed galaxies, at the upper edge of the scatter of the SDSS galaxies. Below we discuss the physical interpretation of this line ratio distribution.

All of these ratios are dependent on the ionisation parameter U and metallicity Z (e.g., Kewley & Dopita 2002; Shirazi et al. 2014; Cameron et al. 2023). In general, R23, R2, and R3 are stronger tracers of Z (e.g., Steidel et al. 2016; Curti et al. 2020), while Ne3O2 and O32 are more dependent on U (e.g., Penston et al. 1990; Levesque & Richardson 2014). The local galaxies observed as part of SDSS show a positive correlation in each diagnostic plot, while the high-redshift galaxies lie at higher O32 and Ne3O2 (suggesting higher U , Cameron et al. 2023). Each region of B14-65666 lies near the intersection of SDSS and previous JWST-observed galaxies.

The metallicity of each region of B14-65666 was found to be $\sim 0.2 - 0.4 Z_{\odot}$ (Section 3.1), allowing us to use these diagrams to compare ionisation states. Since the B14-65666 regions have low O32 and Ne3O2 compared to the other high-redshift sources, this suggests that our sources have relatively low ionisation parameter. The high Z_g and low U (compared to other high-redshift galaxies) suggests that B14-65666 could represent a system of evolved galaxies in the early Universe. Indeed, they lie at the high- Z_g and high- U edge of local galaxies, despite having much less time to evolve.

Since some of the regions of B14-65666 show weak evidence of [OIII] λ 4363 emission (see Figure C1), we also use the O3HG (\equiv [OIII] λ 4363/H γ) vs. O32 AGN diagnostic from Mazzolari et al. (2024). Our best-fit line fluxes yield low O3HG ratios ($\log_{10}(\text{O3HG}) < -0.5$), which suggest that there is no unambiguous AGN signature in B14-65666. While our spectral fits result in low residuals (Figure C1), we note that our fitting routine does not fit [OIII] λ 4363 directly (see Section 3.1.1). Nevertheless, the weak [OIII] λ 4363 in this system does not allow us to confirm or refute the presence of an AGN.

4.2 ALMA-JWST comparison

While JWST is a powerful tool to explore the characteristics of high-redshift galaxies, it also features a strong synergy with ALMA that has not yet been fully explored. This includes the possibility of detecting Lyman continuum leaking galaxies by comparing [C II]158 μ m and [OIII] λ 5007 (e.g., Katz et al. 2020; Ura et al. 2023), using JWST-based gas-phase metallicities and ALMA-based CO observations to derive molecular gas masses (e.g., Narayanan et al. 2012), and comparing [OIII] λ 4959,5007/[O III]88 μ m to place tight constraints on electron temperature (e.g., Stiavelli et al. 2023).

4.2.1 Lyman continuum leakage

The escape of Lyman continuum photons is a key process in the study of how the Universe was reionised, but due to the opacity of the IGM,

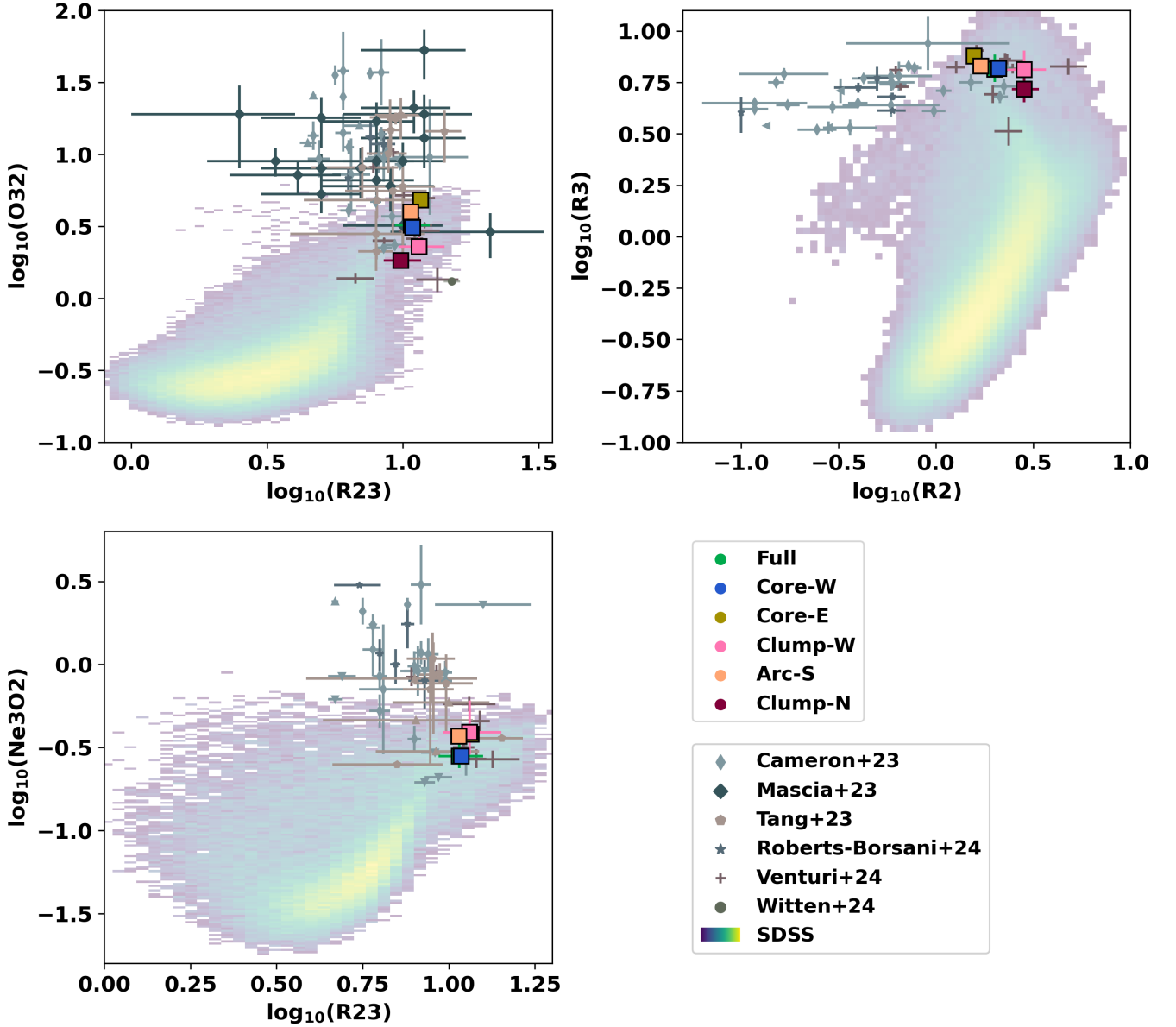


Figure 8. Distribution of line ratios for each galaxy component as measured using circular or elliptical apertures: O32-R23 (top left), R3-R2 (top right), and Ne302-R23 (bottom left). For comparison we also show the locations of low-redshift galaxies from SDSS (MPA-JHU DR8 catalogue; Kauffmann et al. 2003; Brinchmann et al. 2004) and higher redshift galaxies previously observed with JWST/NIRSpec ($5.5 \lesssim z \lesssim 9.5$, Cameron et al. 2023; $4.6 \lesssim z \lesssim 7.9$, Mascia et al. 2023; $6.9 \lesssim z \lesssim 9.0$, Tang et al. 2023; $5 \lesssim z \lesssim 9$, Roberts-Borsani et al. 2024; $6.4 \lesssim z \lesssim 7.9$, Venturi et al. 2024; and $z = 7.88$, Witten et al. 2024).

this quantity is usually explored using indirect tracers (e.g., Izotov et al. 2018; Chisholm et al. 2022; Mascia et al. 2023). A novel approach was proposed by Katz et al. (2020), who used high-resolution cosmological simulations to test the presence of correlations between Lyman continuum escape fraction (hereafter f_{esc}^{LyC}) and a number of strong rest-UV and FIR lines. This resulted in strong evidence for so-called ‘Lyman leakers’ ($f_{esc}^{LyC} > 10\%$) to feature ratios of $I_{[OIII]\lambda 5007}/I_{[CII]158\mu m} > 1$. Since $[CII]158\mu m$ can trace neutral gas (e.g., Vizgan et al. 2022, but see also e.g., Zanella et al. 2018; Madden et al. 2020) and $[OIII]\lambda 5007$ traces ionised gas, a high value of this ratio could indicate a higher level of ionised gas and thus more avenues of escape for Lyman continuum photons. Here, we examine the spatially resolved distribution of this ratio for the first time.

First, we mask all pixels of the $[CII]158\mu m$ integrated flux map

(see Section 3.2.2) that are $< 2\times$ the RMS noise level of the map. The best-fit $[OIII]\lambda 5007$ image (assuming a fiducial PSF of $0.15'' \times 0.15''$; see Section 3.2) is convolved with a 2D Gaussian kernel so that the resulting map has an identical PSF as the ALMA $[CII]158\mu m$ image¹¹. The convolved $[OIII]\lambda 5007$ map is re-gridded to the pixels of the convolved $[CII]158\mu m$ map. Each map is then converted to a uniform set of units ($Jy km s^{-1} arcsec^{-2}$), allowing a direct comparison (Figure 9). We find that this ratio is > 1 for some spaxels in the core regions, providing evidence for higher f_{esc}^{LyC} .

¹¹ The `CREATE_MATCHING_KERNEL` function from the Photutils package (Bradley et al. 2023) is used to determine the appropriate Gaussian kernel to match PSFs.

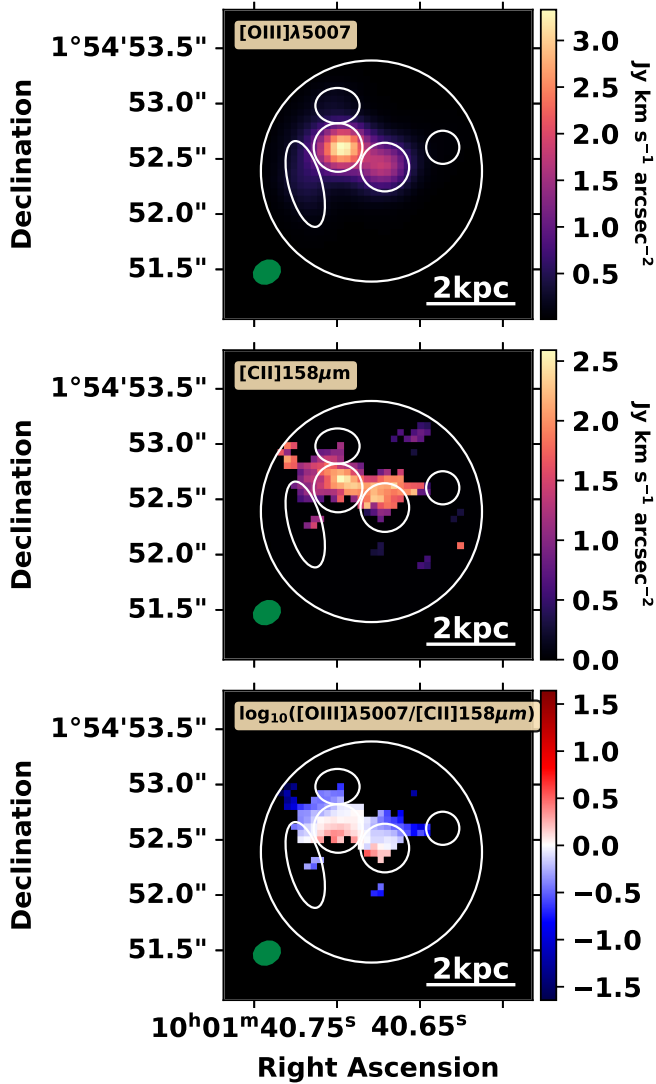


Figure 9. Spatial comparison of $[\text{OIII}]\lambda 5007$ (top panel) and $[\text{CII}]158\mu\text{m}$ emission (middle panel), after each map is convolved to a common PSF and regridded to the same pixel space. The bottom panel shows the ratio of these two maps. Positive values of $\log_{10}([\text{OIII}]\lambda 5007/[\text{CII}]158\mu\text{m})$ (i.e., red spaxels) are possible signatures of Lyman continuum escape.

There also appears to be a north-south gradient, which may indicate asymmetric LyC leakage or astrometric misalignment (see Section 4.2.3)

4.2.2 Electron density

A previous exploration of $[\text{OIII}]\lambda\lambda 4959, 5007/[\text{OIII}]88\mu\text{m}$ was performed by Sugahara et al. (2024), who combined ALMA and JWST/NIRCam observations of B14-65666 to explore how the electron density varies across this source. While these previous observations featured higher spatial resolution, our JWST/NIRSpec data allow us to directly characterise the rest-optical line and continuum emission. We repeat this analysis here using our NIRSpec IFU data.

We convolve the $[\text{OIII}]\lambda\lambda 4959, 5007$ maps with a 2D Gaussian kernel to match the PSF of the $[\text{OIII}]88\mu\text{m}$ map (as derived in Section 3.2.2) and regrid each to a common grid. The resulting ratio

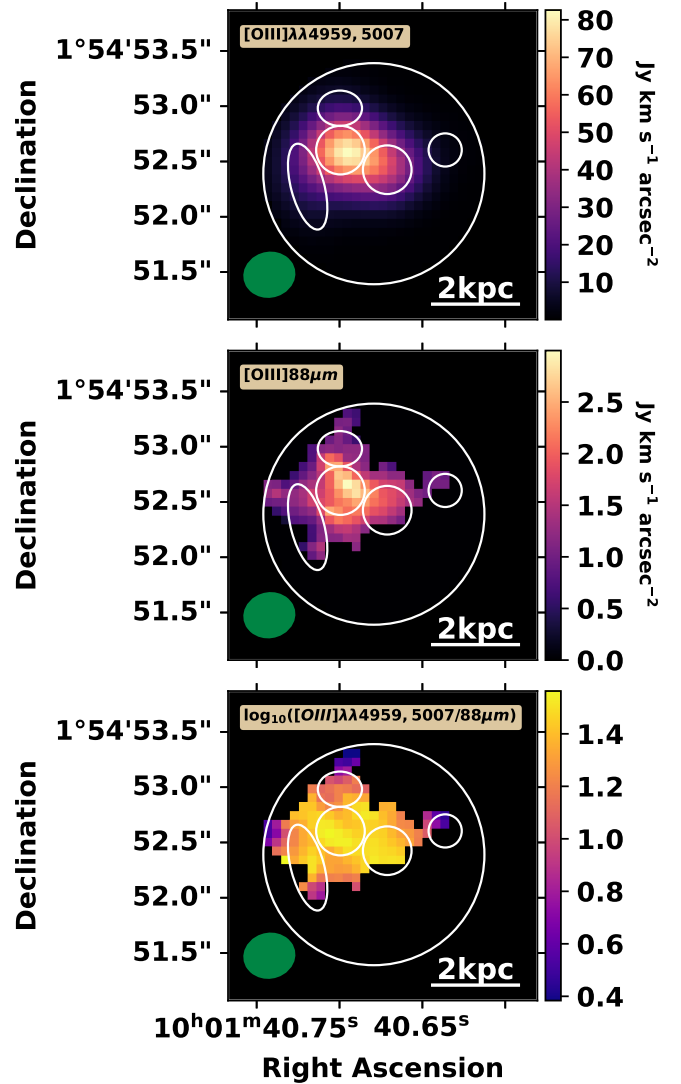


Figure 10. Spatial comparison of $[\text{OIII}]\lambda\lambda 4959, 5007$ (top panel) and $[\text{OIII}]88\mu\text{m}$ emission (middle panel), after each map is convolved to a common PSF and re-gridded to the same pixel space. The bottom panel shows the ratio of these two maps.

map (Figure 10) shows high values in the core regions (~ 1.2), in agreement with that of Sugahara et al. (2024).

Multiple spaxels in Figure 10 show higher ratios (i.e., > 1.3), which would imply $n_e > 10^3$ when combined with the diagnostic plot of Sugahara et al. (2024, see their figure 6). This would have little effect on our results, as the only line ratio with strong n_e dependence ($[\text{OII}]\lambda 3729/[\text{OII}]\lambda 3726$) is unresolved (see PYNEB modelling details of Appendix E). However, our PYNEB modelling shows that this ratio is dependent on both T_e than n_e . Our high observed ratio may then be explained by a slightly higher density and temperature. To investigate this further, we could use higher spectral resolution observations of $[\text{OII}]\lambda\lambda 3726, 3729$ (i.e., JWST/NIRSpec G395H/F290LP) and/or higher spatial resolution observations of $[\text{OIII}]88\mu\text{m}$ (i.e., ALMA).

4.2.3 Note on astrometry

We note that the interpretation of these ratios is dependent on precise astrometric alignment between the JWST/NIRSpec and ALMA

maps, as a misalignment could create a false gradient in the ratio map. From Figure 4, it is clear that the peak of the [C II] $158\mu\text{m}$ emission in Core-E is offset slightly to the northwest from the corresponding peak of [O III] $\lambda 5007$ emission. Here, we explore whether this could cause the observed north-south gradient in [O III] $\lambda 5007$ /[C II] $158\mu\text{m}$ (Figure 9).

If the [C II] $158\mu\text{m}$ map is shifted to the south by 1 px (i.e., $0.06''$), then the observed gradient is no longer present and the highest ratio ($\log_{10}([\text{O III}]\lambda 5007/[\text{C II}]158\mu\text{m}) \sim 0.5$) is $\sim 20\%$ lower. This suggests that the gradient in Figure 9 may be inflated by astrometric uncertainty. However, the [O III] $\lambda\lambda 4959, 5007$ /[O III] $88\mu\text{m}$ ratio map (Figure 10) constructed using our NIRSspec data is similar to that of Sugahara et al. (2024). The latter data are well-aligned (i.e., $< 0.015''$), so the [O III] $88\mu\text{m}$ and [O III] $\lambda\lambda 4959, 5007$ data are likely well-aligned.

In order to avoid this issue of misalignment, we calculate total line ratios by integrating each map. This results in total values of $\log_{10}([\text{O III}]\lambda 5007/[\text{C II}]158\mu\text{m}) = 0.05$ and $\log_{10}([\text{O III}]\lambda\lambda 4959, 5007/[\text{O III}]88\mu\text{m}) = 1.46$. The former suggests that we are not able to determine whether B14-65666 is a Lyman leaker or not (although some regions may feature leakage), and the latter suggests a high electron density (i.e., $\sim 10^3 \text{ cm}^{-3}$; see figure 6 of Sugahara et al. 2024).

4.2.4 Morpho-kinematics

As explored in Sections 3.2.3 and 3.2.4, the ALMA- and JWST-detected lines show flux distributions and kinematics with noteworthy differences. While the JWST-detected lines show emission peaks in both core galaxies, the ALMA-detected lines appear to be focused in Core-E with weaker extensions into Core-W (Figure 4). The v_{50} and w_{80} maps (which are similar to the line of sight velocity and velocity dispersion, respectively) of the narrow component of [O III] $\lambda 5007$ are similar to those of [C II] $158\mu\text{m}$ and [O III] $88\mu\text{m}$, with little evidence for broad emission in the ALMA-detected lines (Figures 5 and 6). Since the ALMA observations resulted in strong detections of each line (Hashimoto et al. 2019), it is unlikely that this disparity is due to a difference of sensitivity.

To explore these differences, we consider a recent comparison of ALMA and JWST/NIRSspec data in the $z = 5.65$ merging system HZ10 (Telikova et al. 2024). Multiple scenarios were put forward to explain areas of low [C II] $158\mu\text{m}$ /[O III] $\lambda 5007$, including a lower carbon abundance as evidenced by a lower Z_g and/or removal of cold gas (an important source of [C II] $158\mu\text{m}$ emission) via photoevaporation. The first scenario is unlikely to explain the absence of [C II] $158\mu\text{m}$ in Core-W, as this region features a higher metallicity than Core-E. The photoevaporation scenario is more likely, as Core-E features a higher U than Core-W.

While we observe that [C II] $158\mu\text{m}$ traces narrow [O III] $\lambda 5007$ emission in B14-65666, the [C II] $158\mu\text{m}$ emission in HZ10 is found to trace broad [O III] $\lambda 5007$ emission (Telikova et al. 2024). This broad emission is interpreted as either outflows or tidal interactions. Similarly, Parlanti et al. (2024a) find evidence for a broad outflow component in [C II] $158\mu\text{m}$ and [O III] $\lambda 5007$ in the $z = 5.54$ galaxy HZ4. To investigate this further, we require deeper ALMA [C II] $158\mu\text{m}$ observations to probe the low-level molecular gas properties, or other JWST observations (e.g., $H\alpha$ with JWST/MIRI) to explore ionised gas properties.

4.3 Presence of dust

The fact that this source is detected in FIR continuum emission with ALMA (e.g., Hashimoto et al. 2019) implies that there is a significant warm dust reservoir in the field. Through a detailed analysis of the dust SED (which has three detections and one non-detection), Sugahara et al. (2021) find a total dust mass of $\sim 10^{6-8} M_{\odot}$ (in agreement with previous results; Hashimoto et al. 2019). The recent SED modelling of Sugahara et al. (2024) found a stellar continuum dust attenuation of $A_V^* = 0.78^{+0.07}_{-0.06}$ (corresponding to ionised gas $E(B - V) \sim 0.4$; Calzetti et al. 2000) for the full source. Our JWST/NIRSspec spectra are well fit by models assuming a low $E(B - V) = 0.2$, but we lack the sensitivity and wavelength coverage necessary to estimate dust attenuation further (See Appendix E3 for further discussion of this).

Briefly, we consider the dust morphology of this field (see Figure 2). Our analysis of the rest-UV and rest-optical line emission shows that these originate primarily from two bright cores, with two much weaker clumps to the north and east, and a weak arc to the south-east. Emission from the rest-FIR lines [C II] $158\mu\text{m}$ and [O III] $88\mu\text{m}$ also is focused in the two core regions. Similarly, the Band 8 continuum emission (underlying [O III] $88\mu\text{m}$ and tracing the peak of the dust SED) originates from Core-W and features a significant diffuse component. But the Band 6 emission (underlying [C II] $158\mu\text{m}$) is focused in a shell-like feature between the two core regions¹². Neither the band 7 nor band 3 maps contain morphological information due to lack of spatial resolution and lack of detection, respectively. Because the emission in each ALMA band is not coincident, it possibly originates from different dust reservoirs.

Since there are three strong rest-FIR continuum detections in this field, the presence of dust is secure. But the fact that the previously studied dust SED was constructed by extracting flux from the full field of B14-65666 from each ALMA band means that the resulting dust masses may be misestimated due to a wavelength-dependent morphology. Indeed, while the modified blackbody model used by Sugahara et al. (2024) is well-tested at high redshift (e.g., Carniani et al. 2019; Jones et al. 2020), it depends on an assumption that the dust emission emerges from a single reservoir characterised by a luminosity-weighted dust temperature, emissivity index, and dust mass. Instead, it may be possible that the FIR emission may emanate from a warmer dust reservoir located in Core-W (see Band 8 image in Figure 2), as well as a colder dust reservoir between the cores (Band 6). Dust temperature gradients have been observed at high redshift (e.g., Calistro Rivera et al. 2018; Dong et al. 2019; Tsukui et al. 2023), which would allow for this change in morphology.

It has previously been found that the viewing angle of galaxies affects the observed dust properties, including attenuation (e.g., Zhang et al. 2023; Lower et al. 2024). These studies analysed simulations of isolated galaxies, but the case of merging galaxies is even more complex due to the presence of companion galaxies and tidal features (e.g., Pallottini et al. 2017; Kohandel et al. 2019). While a spatially resolved FIR SED analysis would unlock a deeper understanding of the warm dust properties and distribution (e.g., Tsukui et al. 2023), it requires time-intensive observations and is currently only feasible for bright sources (e.g., starburst galaxies, QSO host galaxies). With the data available, we may only state that the B14-65666 field contains warm dust that is spatially offset from the bright core regions. This dust may have been expelled by stellar winds (e.g., Veilleux

¹² This morphology was also reported by Hashimoto et al. (2019); Sugahara et al. (2024), and thus is likely not an artefact introduced by our calibration or imaging processes.

et al. 2005), or may be affected by the ongoing galaxy merger (e.g., Tamura et al. 2023).

4.4 Mass-metallicity relation

It has been well established that the properties of most galaxies at a set redshift tend to scale with each other. Examples of this are seen in the observed relations between stellar mass and rotational velocity (i.e., the Tully-Fisher relation; Tully & Fisher 1977), SFR and M_* (star-forming main sequence; Noeske et al. 2007), and the surface densities of molecular and stellar mass (molecular gas main sequence; Lin et al. 2019). Here, we investigate the placement of B14-65666 on the relation between stellar mass and gas-phase metallicity, or the mass-metallicity relation (MZR; Lequeux et al. 1979).

The MZR has been observed for galaxies with a diverse set of redshifts, metallicities, and stellar masses (e.g., Tremonti et al. 2004; Erb et al. 2006; Sanders et al. 2021). Recent JWST observations have enabled measurement of Z_g and M_* in the early Universe, yielding fits of the MZR for galaxies from $7 < z < 10$ and $7.5 < \log_{10}(M_*/M_\odot) < 10.0$ (Heintz et al. 2023), galaxies from the CEERS and JADES surveys from $6 < z < 10$ and $6.0 < \log_{10}(M_*/M_\odot) < 10.0$ (Curti et al. 2024), and galaxies from the CEERS survey from $4 < z < 10$ and $7.2 < \log_{10}(M_*/M_\odot) < 10.1$ (Nakajima et al. 2023). All of these works find that central galaxies with higher stellar masses are more metal enriched, and that the metallicity for a galaxy of a given stellar mass is lower at high redshift than at lower redshifts. There is a scatter between the observed relations, which may be partially explained by the different methods of deriving M_* (i.e. the SED fitting codes BAGPIPES, Carnall et al. 2018; BEAGLE, Chevillard & Charlot 2016; Prospector, Johnson et al. 2021) and Z_g (i.e., strong line diagnostics of Curti et al. 2020; Nakajima et al. 2022).

To examine the location of B14-65666 with respect to the high-redshift MZR, we display Z_g (derived using the line diagnostics of Curti et al. 2020; Section 3.1.2) and M_* (derived by a BAGPIPES fit to the observed SED; Sugahara et al. 2024) for Core-E, Core-W, and the Full aperture in Figure 11. These values are compared to existing best-fit MZR relations (Heintz et al. 2023; Nakajima et al. 2023; Curti et al. 2024) as well as all published $z > 5$ galaxies with Z_g and M_* from JWST/NIRSpec IFU observations (Arribas et al. 2024; Marconcini et al. 2024a,b; Messa et al. 2024; Scholtz et al. 2024; Venturi et al. 2024). We find that the observed galaxies lie above the MZR as derived by Heintz et al. (2023) and Curti et al. (2024), and are closer to the relation of Nakajima et al. (2023).

However, there are important caveats to this interpretation that must be discussed. Primarily, the IFU targets (which mainly originate from the GA-NIFS survey) are not a representative sample of galaxies, but are instead biased towards bright, well-studied objects (e.g., SPT0311-58-E with $\log_{10}(M_*/M_\odot) = 10.55^{+0.05}_{-0.06}$, Arribas et al. 2024). While these observations result in the detection of smaller satellite galaxies (e.g., SPT0311-58-L1 with $\log_{10}(M_*/M_\odot) = 8.54 \pm 0.05$, Arribas et al. 2024), we lack a more complete, unbiased dataset of IFU-detected galaxies in this redshift range ($6 \lesssim z \lesssim 9$). The galaxies at $\log_{10}(M_*/M_\odot) < 7$ originate from the work of Messa et al. (2024), where gravitational magnification ($\mu \sim 20$) allows for the characterisation of dwarf galaxies. The high-metallicity source is SPT0311-58-C3, which lies near the edge of the IFU field of view and thus may suffer from low sensitivity. As noted above, these works also use different methods to derive Z_g and M_* . A uniform analysis of NIRSpec IFU data will be performed in a future work.

We find that B14-65666 is one of the most massive galaxies in our collected sample (second only to the large, clumpy galaxy SPT0311-

58-E; Arribas et al. 2024), but it follows an extrapolation of the Nakajima et al. (2023) MZR trend. This suggests that it does not include a large reservoir of pristine gas (which would result in a lower metallicity), but it is also unlikely to have lost large amounts of gas via outflows or tidal interactions (which would result in a higher metallicity). Instead, it appears that B14-65666 has formed stars and enriched its gas in a similar fashion to other high-redshift galaxies.

4.5 Nature of core components

The two core galaxies of B14-65666 are closely associated, with a projected distance of $\sim 0.43''$ (corresponding to ~ 2.2 kpc) and a velocity offset of ~ 175 km s $^{-1}$. Despite this, their properties reveal a sharp distinction in their natures. On one hand, Core-E appears to have a large molecular reservoir (as suggested by its strong [C II]158 μ m emission; e.g. Zanella et al. 2018; Madden et al. 2020), low Z_g , high SFR (based on H β and [O III]88 μ m; e.g., Arata et al. 2020) and higher ionisation parameter U . With a compact JWST/NIRCam morphology and high M_* , this core likely represents a galaxy undergoing a burst of star formation activity.

Core-W is the opposite in almost every way: it has a lower M_* and amount of molecular gas (i.e., no strong [C II]158 μ m detection), higher Z_g , and little ongoing SF (weaker H β , no significant peak of [O III]88 μ m, lower U). As seen in Figure 11, this core lies above high- z relations, putting it closer to more evolved, lower- z populations. Thus, this core appears to be a galaxy that used its molecular gas in star formation.

Figure 5 shows that there is a clear velocity gradient between these two galaxies, with a broad, redshifted component between them. Such a velocity gradient could be interpreted as a sign of rotation, but this is unlikely here due to the presence of two resolved galaxies (i.e., Core-E and Core-W) with different properties. Since the line and continuum emission peak in one (or both) of the cores rather than between them (except for the ALMA band 6 continuum, see Section 4.3), it is unlikely that this represents a single rotating galaxy, even accounting for the effects of dust obscuration.

Instead, it is likely that these cores represent merging galaxies that have undergone multiple close interactions in the past. Such interactions would strip gas off of each galaxy (explaining the presence of the clumps and arcs), and could boost or lower star formation in each source (e.g., Di Matteo et al. 2008; Horstman et al. 2021; Ellison et al. 2022). The redshifted, broad line emission between the clumps could then represent stripped gas from a previous interaction.

This behaviour has been observed in other systems, such as CR7 (Marconcini et al. 2024a): a $z = 6.6$ field composed of three primary components, an extended Ly α halo, and multiple minor components. A SED fit yielded SF histories (SFHs) for each component, revealing evidence for a past merger-induced starburst. SED fitting of B14-65666 by Sugahara et al. (2024) suggest that the SFH of this field is dominated by a starburst ~ 10 Myr prior to $z = 7.1520$. Additional observations with JWST/MIRI (e.g. to observe H α) or JWST/NIRSpec (e.g., to observe Ly α and enable further SED modelling) could be useful for characterising this field.

5 CONCLUSIONS

In this work, we have presented new JWST/NIRSpec IFU observations of the $z = 7.1520$ galaxy B14-65666 as part of the GA-NIFS survey. Through combination with archival data from JWST/NIRCam and ALMA, we are able to explore the morpho-kinematics and ISM conditions on a spectral and spatial basis.

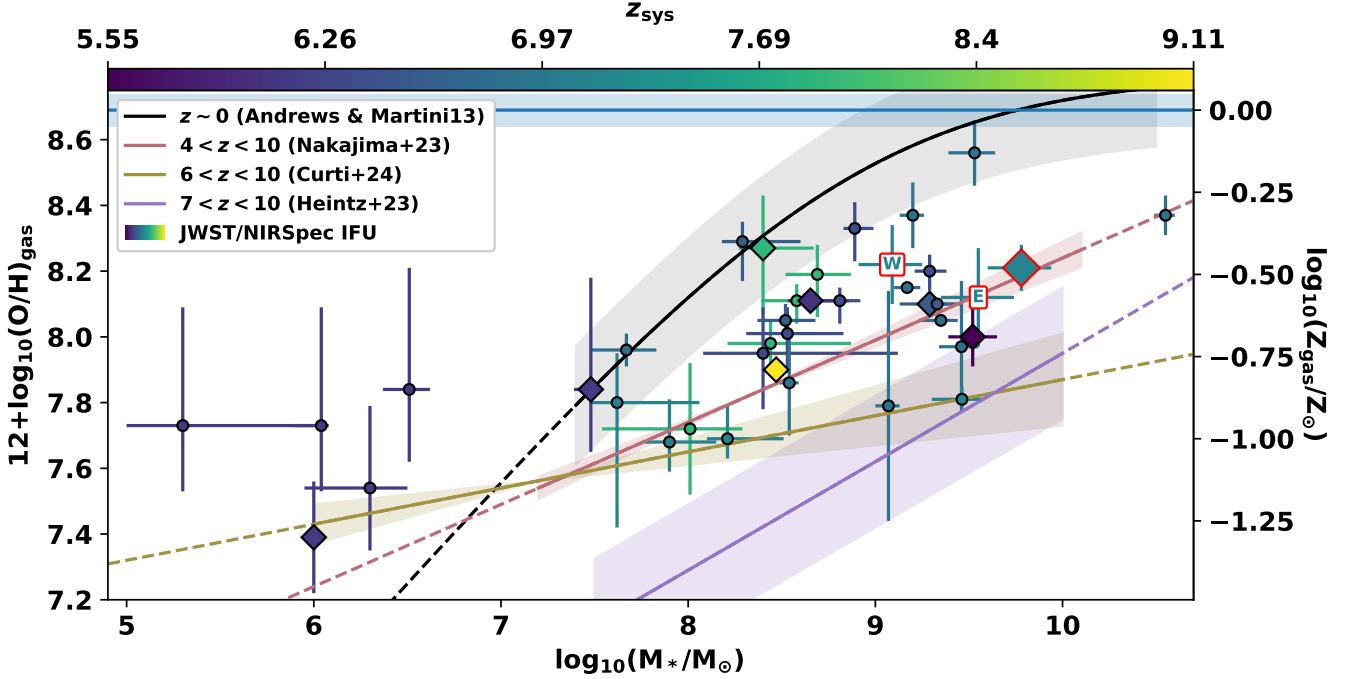


Figure 11. Gas-phase metallicities of $z > 5$ galaxies observed with the JWST/NIRSpec IFU as a function of stellar mass (Übler et al. 2023, 2024a; Arribas et al. 2024; Fujimoto et al. 2024; Ji et al. 2024; Marconcini et al. 2024a,b; Messa et al. 2024; Scholtz et al. 2024; Venturi et al. 2024). Each point is coloured by redshift. Values that represent entire fields rather than regions are shown as diamonds. We also show previously determined MZR fits from local studies (Andrews & Martini 2013) and high-redshift studies (Heintz et al. 2023; Nakajima et al. 2023; Curti et al. 2024). The total value for B14-65666 is shown by a red-outlined diamond, while the values of Core-E and Core-W are shown by ‘E’ and ‘W’, respectively.

We confirm that this object is composed of multiple discrete regions: two bright cores (‘Core-E’ and ‘Core-W’), as well as two small clumps (‘Clump-N’ and ‘Clump-W’) and an extended arc (‘Arc-S’). Spectra extracted from each region reveal significant emission of [OII] $\lambda\lambda 3726, 3729$, [NeIII] $\lambda\lambda 3869, 3968$, [OIII] $\lambda\lambda 4959, 5007$, several Balmer lines ($H\beta$, $H\gamma$, $H\delta$, $H\epsilon$, $H\zeta$), and weak [OIII] $\lambda 4363$. By using `PYNEB` to calculate line ratios for given electron conditions (T_e and n_e), we are able to account for blended lines and the relatively low spectral resolution of the data ($R \sim 1000$). By combining these data with previous ALMA [C II] $158\mu\text{m}$ and [O III] $88\mu\text{m}$ data, we are able to characterise the field with unprecedented detail.

Using strong line diagnostics (Curti et al. 2020), we constrain the gas-phase metallicity of each region to be $\sim 0.2 - 0.4 Z_\odot$. The line ratios of each region lie within the scatter of other $z \sim 5.5 - 9.5$ galaxies observed with JWST/NIRSpec (Cameron et al. 2023; Tang et al. 2023), but with low O32 and Ne3O2 (i.e., low U) and high R23 and R2 (i.e., higher Z_g). Since these properties are more similar to the high-ionisation tail of the distribution of local galaxies observed in SDSS (Kauffmann et al. 2003; Brinchmann et al. 2004), we propose that B14-65666 represents a system of evolved galaxies in the early Universe.

Next, we maximise the potential of our three-dimensional dataset by performing spaxel-by-spaxel fits. This reveals that the emission of each JWST/NIRSpec-detected line is concentrated in the two cores, while the ALMA-detected lines are more focused in Core-E. By fitting the rest-UV and rest-optical lines with a broad and narrow component, we find a region of redshifted, broad emission between the two cores. This likely represents a tidal interaction between the two cores (or possibly an outflow). On the other hand, the narrow emission shows a clear east-west red-blue velocity gradient, which

is also seen in [C II] $158\mu\text{m}$ and [O III] $88\mu\text{m}$. Based on $H\beta$, we find that the star formation is evenly distributed between the narrow and broad components.

The ALMA and JWST data are combined to test optical-FIR line diagnostics, which suggest that B14-65666 may feature regions of high Lyman leakage (although this is found to be dependent on relative astrometry) and may have a high n_e . The differences in ALMA- and JWST-traced morpho-kinematics are explored, and we suggest a few scenarios for mismatches. A comparison of the continuum and line maps suggests that B14-65666 may have a complex dust distribution.

The M_* of B14-65666 (as derived by Sugahara et al. 2024) is combined with our precise estimate of Z_g to examine if this source lies on the high-redshift MZR. By comparing these values with other JWST/NIRSpec IFU-derived values and best-fit trends of representative galaxies, we find that B14-65666 lies on the high-mass edge of the MZR. This suggests the lack of a large molecular reservoir or gas expulsion via feedback.

By combining multiple tracers (e.g., Z_g , $SFR_{H\beta}$, line morpho-kinematics), we determine that the two cores feature drastically different properties. Core-W is a less massive, lower-metallicity galaxy that appears to have already used up its molecular gas reservoir in star formation (based on no significant [C II] $158\mu\text{m}$ peak). Core-E features a higher M_* and SFR , as well as a higher [C II] $158\mu\text{m}$ luminosity, suggesting that this massive system is still evolving. When combined with the kinematics we have observed, the two cores of B14-65666 likely represent a massive merger of two disparate galaxies, which have created tidal features through their past interactions. Through their high Z_g low U (relative to other high-redshift sources), B14-65666 is a massive, merging system in the early Universe.

ACKNOWLEDGEMENTS

G CJ, A JB, and J C acknowledge funding from the “FirstGalaxies” Advanced Grant from the European Research Council (ERC) under the European Union’s Horizon 2020 research and innovation programme (Grant agreement No. 789056). G CJ and J S acknowledge support by the Science and Technology Facilities Council (STFC), by the ERC through Advanced Grant 695671 “QUENCH”, and by the UKRI Frontier Research grant “RISEandFALL.” RB acknowledges support from an STFC Ernest Rutherford Fellowship (ST/T003596/1). SA, MP, and BRdP acknowledge support from Grant PID2021-127718NB-I00 funded by the Spanish Ministry of Science and Innovation/State Agency of Research (MICIN/AEI/10.13039/501100011033). S CA and G V acknowledge support from the European Union (ERC, WINGS, 101040227). H Ū gratefully acknowledges support by the Isaac Newton Trust, the Kavli Foundation through a Newton-Kavli Junior Fellowship, and support through the ERC Starting Grant 101164796 “APEX”. G C acknowledges the support of the INAF Large Grant 2022 “The metal circle: a new sharp view of the baryon cycle up to Cosmic Dawn with the latest generation IFU facilities”. This paper makes use of the following ALMA data: ADS/JAO.ALMA#2015.1.00540.S, ADS/JAO.ALMA#2016.1.00954.S, ADS/JAO.ALMA#2017.1.00190.S, ADS/JAO.ALMA#2018.1.01673.S, ADS/JAO.ALMA#2019.1.01491.S. ALMA is a partnership of ESO (representing its member states), NSF (USA) and NINS (Japan), together with NRC (Canada), MOST and ASIAA (Taiwan), and KASI (Republic of Korea), in cooperation with the Republic of Chile. The Joint ALMA Observatory is operated by ESO, AUI/NRAO and NAOJ.

DATA AVAILABILITY

The JWST/NIRSpec data used in this research has been obtained within the NIRSpec-IFU GTO programme GA-NIFS (PID 1217) and are publicly available on the MAST archive, along with all analysed JWST/NIRCam data. Data presented in this work will be shared upon reasonable request to the corresponding author.

REFERENCES

Andrews B. H., Martini P., 2013, *ApJ*, **765**, 140
 Arata S., Yajima H., Nagamine K., Abe M., Khochfar S., 2020, *MNRAS*, **498**, 5541
 Aravena M., et al., 2024, *A&A*, **682**, A24
 Arribas S., et al., 2024, *A&A*, **688**, A146
 Bañados E., et al., 2018, *Nature*, **553**, 473
 Baker J. G., Menzel D. H., 1938, *ApJ*, **88**, 52
 Baldwin J. A., Phillips M. M., Terlevich R., 1981, *PASP*, **93**, 5
 Béthermin M., Doré O., Lagache G., 2012, *A&A*, **537**, L5
 Böker T., et al., 2022, *A&A*, **661**, A82
 Bowler R. A. A., et al., 2012, *MNRAS*, **426**, 2772
 Bowler R. A. A., et al., 2014, *MNRAS*, **440**, 2810
 Bowler R. A. A., Dunlop J. S., McLure R. J., McLeod D. J., 2017, *MNRAS*, **466**, 3612
 Bowler R. A. A., Bourne N., Dunlop J. S., McLure R. J., McLeod D. J., 2018, *MNRAS*, **481**, 1631
 Bowler R. A. A., Cullen F., McLure R. J., Dunlop J. S., Avison A., 2022, *MNRAS*, **510**, 5088
 Boyett K., et al., 2024, *MNRAS*, **535**, 1796
 Bradley L., et al., 2023, *astropy/photutils: 1.7.0*, doi:10.5281/zenodo.7804137

Brinchmann J., Charlot S., White S. D. M., Tremonti C., Kauffmann G., Heckman T., Brinkmann J., 2004, *MNRAS*, **351**, 1151
 Calistro Rivera G., et al., 2018, *ApJ*, **863**, 56
 Calzetti D., Armus L., Bohlin R. C., Kinney A. L., Koornneef J., Storchi-Bergmann T., 2000, *ApJ*, **533**, 682
 Cameron A. J., et al., 2023, *A&A*, **677**, A115
 Caputi K. I., et al., 2017, *ApJ*, **849**, 45
 Carnall A. C., McLure R. J., Dunlop J. S., Davé R., 2018, *MNRAS*, **480**, 4379
 Carniani S., et al., 2018, *MNRAS*, **478**, 1170
 Carniani S., et al., 2019, *MNRAS*, **489**, 3939
 Carniani S., et al., 2024a, *arXiv e-prints*, p. arXiv:2409.20533
 Carniani S., et al., 2024b, *Nature*, **633**, 318
 Chabrier G., 2003, *PASP*, **115**, 763
 Chen Z., Stark D. P., Mason C., Topping M. W., Whitler L., Tang M., Endsley R., Charlot S., 2024, *MNRAS*, **528**, 7052
 Chevallard J., Charlot S., 2016, *MNRAS*, **462**, 1415
 Chisholm J., et al., 2022, *MNRAS*, **517**, 5104
 Chisholm J., et al., 2024, *MNRAS*, **534**, 2633
 Claude S., et al., 2008, in Duncan W. D., Holland W. S., Withington S., Zmuidzinas J., eds, *Society of Photo-Optical Instrumentation Engineers (SPIE) Conference Series Vol. 7020, Millimeter and Submillimeter Detectors and Instrumentation for Astronomy IV*. p. 70201B, doi:10.1117/12.788128
 Comparat J., Kneib J.-P., Bacon R., Mostek N. J., Newman J. A., Schlegel D. J., Yèche C., 2013, *A&A*, **559**, A18
 Curti M., Mannucci F., Cresci G., Maiolino R., 2020, *MNRAS*, **491**, 944
 Curti M., et al., 2023, *MNRAS*, **518**, 425
 Curti M., et al., 2024, *A&A*, **684**, A75
 Curtis-Lake E., et al., 2023, *Nature Astronomy*, **7**, 622
 D’Eugenio F., et al., 2024a, *arXiv e-prints*, p. arXiv:2404.06531
 D’Eugenio F., et al., 2024b, *Nature Astronomy*, **8**, 1443
 Decarli R., et al., 2024, *A&A*, **689**, A219
 Di Matteo P., Bournaud F., Martig M., Combes F., Melchior A. L., Semelin B., 2008, *A&A*, **492**, 31
 Díaz A. I., Castellanos M., Terlevich E., Luisa García-Vargas M., 2000, *MNRAS*, **318**, 462
 Dong C., et al., 2019, *ApJ*, **873**, 50
 Driver S. P., Robotham A. S. G., Bland-Hawthorn J., Brown M., Hopkins A., Liske J., Phillipps S., Wilkins S., 2013, *MNRAS*, **430**, 2622
 Duan Q., et al., 2024, *arXiv e-prints*, p. arXiv:2411.04944
 Dutton A. A., van den Bosch F. C., Dekel A., 2010, *MNRAS*, **405**, 1690
 Ediss G. A., et al., 2004, in Narayanan G., ed., *Fifteenth International Symposium on Space Terahertz Technology*. pp 181–188
 Ellison S. L., et al., 2022, *MNRAS*, **517**, L92
 Emerson J. P., Sutherland W. J., 2010, in Stepp L. M., Gilmozzi R., Hall H. J., eds, *Society of Photo-Optical Instrumentation Engineers (SPIE) Conference Series Vol. 7733, Ground-based and Airborne Telescopes III*. p. 773306, doi:10.1117/12.857105
 Erb D. K., Shapley A. E., Pettini M., Steidel C. C., Reddy N. A., Adelberger K. L., 2006, *ApJ*, **644**, 813
 Fan X., et al., 2001, *AJ*, **122**, 2833
 Ferland G. J., Korista K. T., Verner D. A., Ferguson J. W., Kingdon J. B., Verner E. M., 1998, *PASP*, **110**, 761
 Ferland G. J., et al., 2017, *Rev. Mex. Astron. Astrofis.*, **53**, 385
 Figueira M., et al., 2022, *A&A*, **667**, A29
 Flores Velázquez J. A., et al., 2021, *MNRAS*, **501**, 4812
 Fujimoto S., et al., 2024, *arXiv e-prints*, p. arXiv:2402.18543
 Gaia Collaboration et al., 2016, *A&A*, **595**, A1
 Gaia Collaboration et al., 2021, *A&A*, **649**, A1
 Gardner J. P., et al., 2023, *PASP*, **135**, 068001
 González V., Labbé I., Bouwens R. J., Illingworth G., Franx M., Kriek M., Brammer G. B., 2010, *ApJ*, **713**, 115
 Gruppioni C., et al., 2020, *A&A*, **643**, A8
 Hashimoto T., et al., 2019, *PASJ*, **71**, 71
 Hashimoto T., et al., 2023a, *ApJ*, **952**, 48
 Hashimoto T., et al., 2023b, *ApJ*, **955**, L2
 Heintz K. E., et al., 2023, *Nature Astronomy*, **7**, 1517

- Herrera-Camus R., et al., 2022, *A&A*, **665**, L8
- Hodge J. A., Carilli C. L., Walter F., de Blok W. J. G., Riechers D., Daddi E., Lentati L., 2012, *ApJ*, **760**, 11
- Horstman K., et al., 2021, *MNRAS*, **501**, 137
- Hsiao T. Y.-Y., et al., 2024a, *ApJ*, **973**, 8
- Hsiao T. Y.-Y., et al., 2024b, *ApJ*, **973**, 81
- Hu E. M., Cowie L. L., McMahon R. G., Capak P., Iwamuro F., Kneib J. P., Maihara T., Motohara K., 2002, *ApJ*, **568**, L75
- Hu W., et al., 2024, *ApJ*, **971**, 21
- Isobe Y., Ouchi M., Nakajima K., Harikane Y., Ono Y., Xu Y., Zhang Y., Umeda H., 2023, *ApJ*, **956**, 139
- Izotov Y. I., Worseck G., Schaerer D., Guseva N. G., Thuan T. X., Fricke Verhamme A., Orlitová I., 2018, *MNRAS*, **478**, 4851
- Jakobsen P., et al., 2022, *A&A*, **661**, A80
- Ji X., et al., 2024, *MNRAS*, **535**, 881
- Johnson B. D., Leja J., Conroy C., Speagle J. S., 2021, *ApJS*, **254**, 22
- Jones G. C., et al., 2017, *ApJ*, **850**, 180
- Jones G. C., Maiolino R., Caselli P., Carniani S., 2020, *MNRAS*, **498**, 4109
- Jones G. C., et al., 2021, *MNRAS*, **507**, 3540
- Jones G. C., et al., 2024a, *arXiv e-prints*, p. [arXiv:2405.12955](https://arxiv.org/abs/2405.12955)
- Jones G. C., et al., 2024b, *A&A*, **682**, A122
- Katz H., et al., 2020, *MNRAS*, **498**, 164
- Kauffmann G., et al., 2003, *MNRAS*, **341**, 33
- Kennicutt Robert C. J., 1998, *ApJ*, **498**, 541
- Kerr A. R., et al., 2004, in Narayanan G., ed., *Fifteenth International Symposium on Space Terahertz Technology*. pp 55–61
- Kerr A. R., Pan S.-K., Claude S. M. X., Dindo P., Lichtenberger A. W., Efland J. E., Lauria E. F., 2014, *IEEE Transactions on Terahertz Science and Technology*, **4**, 201
- Kewley L. J., Dopita M. A., 2002, *ApJS*, **142**, 35
- Kewley L. J., Nicholls D. C., Sutherland R., Rigby J. R., Acharya A., Dopita M. A., Bayliss M. B., 2019, *ApJ*, **880**, 16
- Khusanova Y., et al., 2021, *A&A*, **649**, A152
- Kohandel M., Pallottini A., Ferrara A., Zanella A., Behrens C., Carniani S., Gallerani S., Vallini L., 2019, *MNRAS*, **487**, 3007
- Kokorev V., et al., 2024, *arXiv e-prints*, p. [arXiv:2411.13640](https://arxiv.org/abs/2411.13640)
- Lamperti I., et al., 2024, *A&A*, **691**, A153
- Laporte N., Meyer R. A., Ellis R. S., Robertson B. E., Chisholm J., Roberts-Borsani G. W., 2021, *MNRAS*, **505**, 3336
- Lelli F., Di Teodoro E. M., Fraternali F., Man A. W. S., Zhang Z.-Y., De Breuck C., Davis T. A., Maiolino R., 2021, *Science*, **371**, 713
- Lequeux J., Peimbert M., Rayo J. F., Serrano A., Torres-Peimbert S., 1979, *A&A*, **80**, 155
- Levesque E. M., Richardson M. L. A., 2014, *ApJ*, **780**, 100
- Li Q., Narayanan D., Davé R., 2019, *MNRAS*, **490**, 1425
- Lin L., et al., 2019, *ApJ*, **884**, L33
- Liu W., et al., 2024, *ApJ*, **976**, 33
- Longhetti M., Saracco P., 2009, *MNRAS*, **394**, 774
- Looser T. J., et al., 2024, *Nature*, **629**, 53
- Lower S., Narayanan D., Hu C.-Y., Privon G. C., 2024, *ApJ*, **965**, 123
- Luridiana V., Morisset C., Shaw R. A., 2015, *A&A*, **573**, A42
- Lyu J., et al., 2024, *arXiv e-prints*, p. [arXiv:2412.04548](https://arxiv.org/abs/2412.04548)
- Madau P., Dickinson M., 2014, *ARA&A*, **52**, 415
- Madden S. C., et al., 2020, *A&A*, **643**, A141
- Mahieu S., et al., 2012, *IEEE Transactions on Terahertz Science and Technology*, **2**, 29
- Marconcini C., et al., 2024a, *arXiv e-prints*, p. [arXiv:2411.08627](https://arxiv.org/abs/2411.08627)
- Marconcini C., et al., 2024b, *MNRAS*, **533**, 2488
- Marshall M. A., et al., 2023, *A&A*, **678**, A191
- Marshall M. A., et al., 2024, *arXiv e-prints*, p. [arXiv:2410.11035](https://arxiv.org/abs/2410.11035)
- Mascia S., et al., 2023, *A&A*, **672**, A155
- Mazzolari G., et al., 2024, *A&A*, **691**, A345
- McCracken H. J., et al., 2012, *A&A*, **544**, A156
- Messa M., et al., 2024, *arXiv e-prints*, p. [arXiv:2407.20331](https://arxiv.org/abs/2407.20331)
- Nagao T., Maiolino R., Marconi A., 2006, *A&A*, **459**, 85
- Nakajima K., et al., 2022, *ApJS*, **262**, 3
- Nakajima K., Ouchi M., Isobe Y., Harikane Y., Zhang Y., Ono Y., Umeda H., Oguri M., 2023, *ApJS*, **269**, 33
- Narayanan D., Krumholz M. R., Ostriker E. C., Hernquist L., 2012, *MNRAS*, **421**, 3127
- Neeleman M., Prochaska J. X., Kanekar N., Rafelski M., 2020, *Nature*, **581**, 269
- Newville M., Stensitzki T., Allen D. B., Ingarciola A., 2014, *LMFIT: Non-Linear Least-Square Minimization and Curve-Fitting for Python*, doi:[10.5281/zenodo.11813](https://doi.org/10.5281/zenodo.11813)
- Noeske K. G., et al., 2007, *ApJ*, **660**, L43
- Pallottini A., Ferrara A., Gallerani S., Vallini L., Maiolino R., Salvadori S., 2017, *MNRAS*, **465**, 2540
- Pallottini A., et al., 2022, *MNRAS*, **513**, 5621
- Panther B., Jimenez R., Heavens A. F., Charlot S., 2007, *MNRAS*, **378**, 1550
- Papovich C., et al., 2022, *ApJ*, **937**, 22
- Parlanti E., et al., 2024a, *arXiv e-prints*, p. [arXiv:2407.19008](https://arxiv.org/abs/2407.19008)
- Parlanti E., et al., 2024b, *A&A*, **684**, A24
- Penston M. V., et al., 1990, *A&A*, **236**, 53
- Perna M., et al., 2023, *A&A*, **679**, A89
- Ragone-Figueroa C., Granato G. L., Parente M., Murante G., Valentini M., Borgani S., Maio U., 2024, *A&A*, **691**, A200
- Reddy N. A., et al., 2018, *ApJ*, **869**, 92
- Reddy N. A., et al., 2022, *ApJ*, **926**, 31
- Reddy N. A., Topping M. W., Sanders R. L., Shapley A. E., Brammer G., 2023, *ApJ*, **952**, 167
- Riechers D. A., et al., 2019, *ApJ*, **872**, 7
- Rigby J., et al., 2023, *PASP*, **135**, 048001
- Roberts-Borsani G., et al., 2024, *ApJ*, **976**, 193
- Rodríguez Del Pino B., et al., 2024, *A&A*, **684**, A187
- Rowland L. E., et al., 2024, *MNRAS*, **535**, 2068
- Salpeter E. E., 1955, *ApJ*, **121**, 161
- Sanders R. L., et al., 2016, *ApJ*, **816**, 23
- Sanders R. L., et al., 2021, *ApJ*, **914**, 19
- Saxena A., et al., 2023, *A&A*, **678**, A68
- Scarlata C., Hayes M., Panagia N., Mehta V., Haardt F., Bagley M., 2024, *arXiv e-prints*, p. [arXiv:2404.09015](https://arxiv.org/abs/2404.09015)
- Scholtz J., et al., 2024, *arXiv e-prints*, p. [arXiv:2411.07695](https://arxiv.org/abs/2411.07695)
- Scoville N., et al., 2007, *ApJS*, **172**, 1
- Sekimoto Y., Iizuko Y., Satou N., Ito T., Kumagai K., Kamikura M., Naruse M., Shan W. L., 2008, in Wild W., ed., *Nineteenth International Symposium on Space Terahertz Technology*. pp 253–257
- Shirazi M., Brinchmann J., Rahmati A., 2014, *ApJ*, **787**, 120
- Smit R., et al., 2018, *Nature*, **553**, 178
- Solimano M., et al., 2024, *arXiv e-prints*, p. [arXiv:2407.13020](https://arxiv.org/abs/2407.13020)
- Stanway E. R., Bunker A. J., McMahon R. G., 2003, *MNRAS*, **342**, 439
- Steidel C. C., Strom A. L., Pettini M., Rudie G. C., Reddy N. A., Trainor R. F., 2016, *ApJ*, **826**, 159
- Stiavelli M., et al., 2023, *ApJ*, **957**, L18
- Sugahara Y., et al., 2021, *ApJ*, **923**, 5
- Sugahara Y., et al., 2024, *arXiv e-prints*, p. [arXiv:2403.17133](https://arxiv.org/abs/2403.17133)
- Tacchella S., et al., 2022, *MNRAS*, **513**, 2904
- Tamura Y., et al., 2023, *ApJ*, **952**, 9
- Tang M., et al., 2023, *MNRAS*, **526**, 1657
- Taniguchi Y., et al., 2005, *PASJ*, **57**, 165
- Telikova K., et al., 2024, *arXiv e-prints*, p. [arXiv:2411.09033](https://arxiv.org/abs/2411.09033)
- Torralba-Torregrosa A., et al., 2024, *A&A*, **689**, A44
- Traina A., et al., 2024, *A&A*, **681**, A118
- Tremonti C. A., et al., 2004, *ApJ*, **613**, 898
- Tskui T., Wisnioski E., Krumholz M. R., Battisti A., 2023, *MNRAS*, **523**, 4654
- Tully R. B., Fisher J. R., 1977, *A&A*, **54**, 661
- Übler H., et al., 2023, *A&A*, **677**, A145
- Übler H., et al., 2024a, *MNRAS*, **531**, 355
- Übler H., et al., 2024b, *MNRAS*, **533**, 4287
- Ulivi L., et al., 2024, *arXiv e-prints*, p. [arXiv:2407.08505](https://arxiv.org/abs/2407.08505)
- Ura R., et al., 2023, *ApJ*, **948**, 3
- Veilleux S., Osterbrock D. E., 1987, *ApJS*, **63**, 295
- Veilleux S., Cecil G., Bland-Hawthorn J., 2005, *ARA&A*, **43**, 769
- Venturi G., et al., 2024, *A&A*, **691**, A19

Vizgan D., Heintz K. E., Greve T. R., Narayanan D., Davé R., Olsen K. P., Popping G., Watson D., 2022, *ApJ*, 939, L1
 Witstok J., Smit R., Maiolino R., Curti M., Laporte N., Massey R., Richard J., Swinbank M., 2021, *MNRAS*, 508, 1686
 Witstok J., et al., 2024, *arXiv e-prints*, p. arXiv:2408.16608
 Witten C., et al., 2024, *arXiv e-prints*, p. arXiv:2407.07937
 Zamora S., et al., 2024, *arXiv e-prints*, p. arXiv:2412.02751
 Zanella A., et al., 2018, *MNRAS*, 481, 1976
 Zhang J., et al., 2023, *MNRAS*, 524, 4128

APPENDIX A: NIRCAM-NIRSPEC FLUX COMPARISON

In Section 2, we corrected the astrometry of our NIRSpec IFU data by convolving our cube with NIRCcam spectral filters and comparing the resulting images with the observed NIRCcam images. We may further exploit this synergy by comparing the extracted fluxes of each image.

The only hindrance is the use of different flux units: $\text{erg s}^{-1} \text{cm}^{-2} \text{\AA}^{-1}$ for the NIRSpec images, and MJy sr^{-1} for the NIRCcam images. To enable a common comparison, we take our NIRSpec data cube and convert each value in the cube to have units of MJy sr^{-1} :

$$\frac{F_{\nu,i}(x,y)}{[\text{MJy sr}^{-1}]} = \frac{10^{27} \lambda^2 180^2}{c \pi^2 A_{px}} \frac{F_{\lambda,i}(x,y)}{[\text{erg s}^{-1} \text{cm}^{-2} \text{\AA}^{-1}]} \quad (\text{A1})$$

where i represents a spectral bin, λ is the observed-frame wavelength [m], c is the speed of light [m s^{-1}], and A_{px} is the area of each spaxel [square degrees]. This converted cube is then convolved with the transmission curve of each NIRCcam filter (which includes all system throughputs)¹³ to create a map that is comparable to the NIRCcam image:

$$F_{\nu,Conv}(x,y)[\text{MJy sr}^{-1}] = \frac{\sum_i F_{\nu,i}(x,y) f(v_i) \Delta v_i}{\sum_i f(v_i) \Delta v_i} \quad (\text{A2})$$

where $f(v_i)$ is the filter transmission curve, interpolated to the same spectral bins as the data.

This procedure is used to create F356W and F444W images from the NIRSpec data cube. Extracting the flux from the ‘Full’ aperture of Figure 2, we find that the F444W images only differ by $\sim 1\%$ in great agreement, while the F356W images are more discrepant ($\sim 10\%$ deviation). A closer look reveals that the NIRSpec F356W image features significant noise artefacts (i.e., stripes of enhanced signal along central detector rows) that inflate the extracted flux. Future reductions with stronger artefact removal may reduce this difference. For now, we find no significant systemic difference between the NIRSpec and NIRCcam fluxes.

APPENDIX B: JWST/NIRCAM ASTROMETRY

In Section 2.1, we use archival JWST/NIRCcam images to align our JWST/NIRSpec data cubes (see Figure 1). However, it is worthwhile to discuss the absolute reliability of this alignment. Sugahara et al. (2024) analysed these JWST/NIRCcam images in depth, noting that while they required an astrometric correction to align with three stars in the *Gaia* DR3 catalogue (Gaia Collaboration et al. 2016, 2021), the resulting corrected images had very low astrometric uncertainties ($< 0.015''$). Here, we search for emission at the location of the three

¹³ <https://jwst-docs.stsci.edu/jwst-near-infrared-camera/nircam-instrumentation/nircam-filters>

Table B1. Positions of the three objects in the *Gaia* archive in the field of view of the JWST/NIRCcam images studied here.

Number	RA [°]	Dec [°]
1	150.42848680589384	1.9132852051973277
2	150.42771191175737	1.9072885668107642
3	150.44513364015506	1.9126676038888937

Gaia star locations (Table B1) in each JWST/NIRCcam image (see Section 2.2).

As seen in Figure B1, the JWST/NIRCcam images have excellent alignment to each other and feature significant emission near the locations of all three *Gaia* stars. Objects #1 and #2 are well aligned, with offsets from the *Gaia* frame of $< 0.1''$ in all JWST/NIRCcam images. On the other hand, it appears that object #3 features a larger offset ($\sim 0.2''$). The origin of this larger offset is not apparent (e.g., calibration error), but the fact that we do not see a systematic offset between the *Gaia* DR3 positions and JWST/NIRCcam emission suggests that our absolute astrometry is trustworthy to within $0.2''$.

APPENDIX C: BEST-FIT INTEGRATED SPECTRA

In Section 3.1, we extracted spectra from each region and fit them with combined line and continuum models. Here, we present the extracted spectra, best fit models (including the narrow and broad components), and residuals for each spectrum (Figures C1 and C1). See Section 3.1.1 for full description of our modelling procedure.

APPENDIX D: NARROW AND BROAD MAPS

In the main text (Section 3.2), we characterised the B14-65666 field on a resolved basis by extracting the spectrum from each spaxel and fitting it with a line and continuum model (see Section 3.1.1). This model contains contributions from both a broad and narrow component, but we only show the total fits in Section 3.2. Here, we show the best-fit integrated intensities of each component, as well as the line diagnostics (Figure D1)

APPENDIX E: LINE RATIO DETERMINATION

Throughout this work, we use line ratios derived using PYNEB. This allows us to self-consistently fit and analyse line emission using a single framework. The details of these assumptions are given here.

E1 Dust-free line ratios

One vital pair of ISM properties are the electron density and temperature. The electron density in galaxies has been derived for $z \sim 2.3$ galaxies ($n_e = 250 \text{ cm}^{-3}$; e.g. Sanders et al. 2016), as well as for $z > 6$ galaxies using JWST data ($n_e = 100 - 500 \text{ cm}^{-3}$; e.g. Curti et al. 2023; Nakajima et al. 2023; Chen et al. 2024; Hu et al. 2024; Torralba-Torregrosa et al. 2024). More generally, Isobe et al. (2023) characterise the redshift evolution of n_e , yielding a range of $n_e \sim 200 - 1000 \text{ cm}^{-3}$ for a source at $z \sim 7$. Below we will explore a range of $n_e = 100 - 1000 \text{ cm}^{-3}$ (as suggested by Tang et al. 2023).

Similarly, the electron temperature is found to be $\sim 1.5 \times 10^4 \text{ K}$ for high-redshift sources (e.g., Hsiao et al. 2024b; Hu et al. 2024; Torralba-Torregrosa et al. 2024). While a broad range of $T_e = [0.5 - 20] \times 10^4 \text{ K}$ is explored by Chen et al. (2024), we restrict

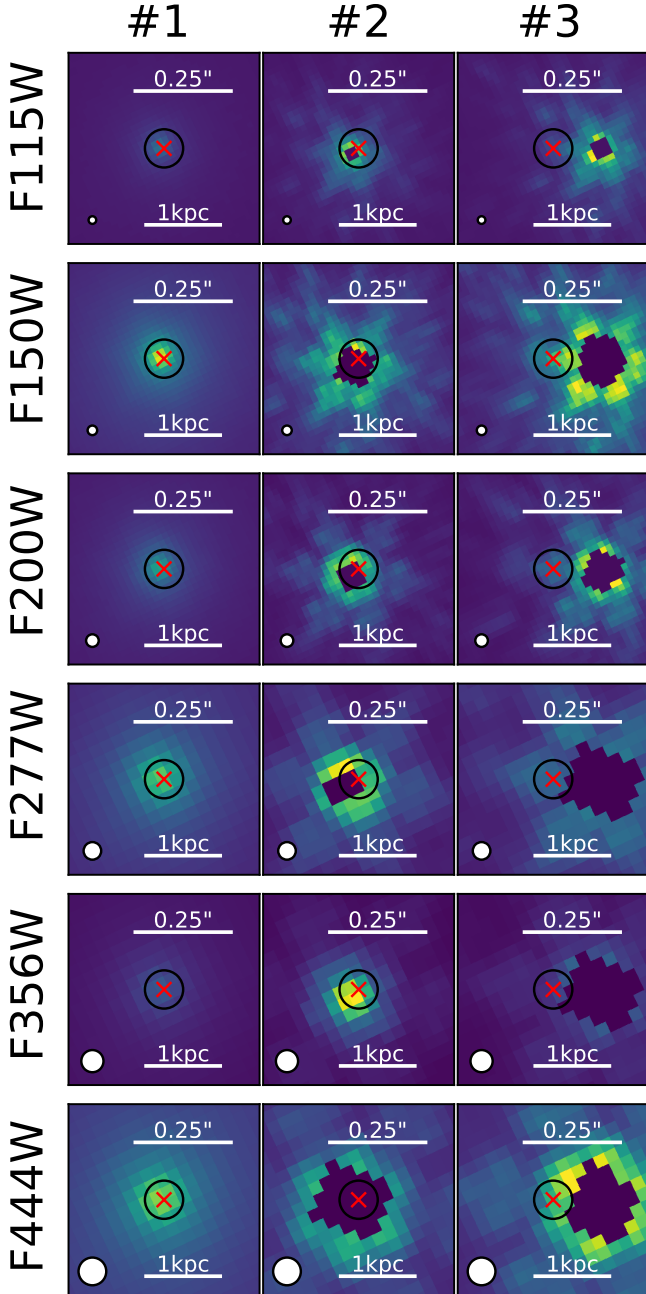


Figure B1. Comparison of JWST/NIRCam data with positions of three stars from the *Gaia* DR3 catalogue. Each panel contains a $2'' \times 2''$ view of a JWST/NIRCam image (see the labels for each row for filter) centred on a given location from the *Gaia* archive (see the labels for each column). The *Gaia* position is shown as a red X and a black circle of radius $0.1''$ (corresponding to the JWST pointing uncertainty; Rigby et al. 2023). The PSF is shown as a circle to the lower left.

our exploration to temperatures where `PYNEB` is able to calculate each dust-corrected Balmer ratio ($T_e = [0.5 - 3.0] \times 10^4$ K).

Previously, Sugahara et al. (2024) assumed $T_e = 1.2 \times 10^4$ K and $n_e = 200 \text{ cm}^{-3}$ when interpreting JWST/NIRCam observations of B14-65666. Through a comparison of the observed $[\text{OIII}]\lambda\lambda 4959, 5007 / [\text{O III}]\lambda 88\mu\text{m}$ ratio to results from `CLOUDY` (Ferland et al. 1998, 2017), they were able to rule out low ($< 100 \text{ cm}^{-3}$) and high electron densities ($> 10^3 \text{ cm}^{-3}$). For our exploration, we

Line Ratio	$E(B - V)$	$E(B - V)$
	0.0	0.2
$\text{H}\alpha/\text{H}\beta$	2.828	3.574
$\text{H}\gamma/\text{H}\beta$	0.471	0.427
$\text{H}\delta/\text{H}\beta$	0.261	0.225
$\text{H}\epsilon/\text{H}\beta$	0.160	0.134
$\text{H}\zeta/\text{H}\beta$	0.106	0.087
$[\text{OIII}]\lambda 5007 / [\text{OIII}]\lambda 4959$	2.984	3.008
$[\text{OII}]\lambda 3729 / [\text{OII}]\lambda 3726$	1.246	1.246
$\log_{10}([\text{OIII}]\lambda\lambda 4959, 5007 / [\text{O III}]\lambda 88\mu\text{m})$	0.924	0.566
$\log_{10}([\text{OIII}]\lambda\lambda 4959, 5007 / [\text{OIII}]\lambda 4363)$	2.073	2.123
$[\text{NeIII}]\lambda 3968 / [\text{NeIII}]\lambda 3869$	0.301	0.308

Table E1. Dust-corrected line ratios found using `PYNEB` using fiducial electron properties ($n_e = 200 \text{ cm}^{-3}$ and $T_e = 1.2 \times 10^4$ K) and either $E(B - V) = 0$ (central column) or $E(B - V) = 0.2$ (right column). Italicised entries are independent of density and temperature.

mark the locations of these fiducial values of $n_e = 200 \text{ cm}^{-3}$ and $T_e = 1.2 \times 10^4$ K in each plot, and the resulting ratio values are listed in Table E1.

First, we explore Balmer line ratios using the `PYNEB` task *getEmissivity*. The resulting distribution of $\text{H}\gamma/\text{H}\beta$ values (first panel of Figure E1) shows that this ratio features a much stronger dependence on T_e than n_e . The other Balmer ratios show a similar dependence on T_e , with a $< 6\%$ deviations from their fiducial value over our explored parameter space.

Next, we explore the range of multiple oxygen line ratios. The first ratio ($[\text{OIII}]\lambda 5007 / [\text{OIII}]\lambda 4959$) is fixed by atomic physics and therefore does not vary with n_e or T_e . On the other hand, $[\text{OII}]\lambda 3726 / [\text{OII}]\lambda 3729$ is strongly dependent on n_e , $([\text{OIII}]\lambda\lambda 4959, 5007 / [\text{OIII}]\lambda 4363)$ is dependent on T_e , and $([\text{OIII}]\lambda\lambda 4959, 5007 / [\text{O III}]\lambda 88\mu\text{m})$ is dependent on both parameters. Due to the large variation in the latter two ratios (i.e., more than 1 dex), we present the logarithm of each in Figure E1.

Like $[\text{OIII}]\lambda 5007 / [\text{OIII}]\lambda 4959$, the ratio $[\text{NeIII}]\lambda 3869 / [\text{NeIII}]\lambda 3968$ is fixed by atomic physics, and thus is not dependent on n_e or T_e . Because of this, we present the fiducial value in Table E1 but do not show a distribution.

E2 Dust reddening

In addition, line ratios may be affected by dust extinction. In the case of a dust-free environment, $E(B - V) = 0$, and the line ratios discussed in the previous subsection would be appropriate. However, even for $E(B - V) \leq 0.5$, line ratios will differ significantly from their extinction-free values (see Equation 1). To demonstrate this, Figure E2 shows the $T_e - E(B - V)$ grid for $\text{H}\gamma/\text{H}\beta$, $[\text{OIII}]\lambda 5007 / [\text{OIII}]\lambda 4959$, and $[\text{NeIII}]\lambda 3968 / [\text{NeIII}]\lambda 3869$.

For each of the Balmer ratios, it is clear that for the range of parameters considered, $E(B - V)$ has more of an effect on the observed ratio than T_e . This is also true for the oxygen and neon ratios, which are temperature-independent. While the oxygen and neon ratios only vary a few percent from the fiducial values ($\leq 3\%$), the Balmer ratios have larger variations that increase with transition number (e.g., $\sim 15\%$ for $\text{H}\gamma/\text{H}\beta$ and $\sim 30\%$ for $\text{H}\zeta/\text{H}\beta$).

E3 Line ratio interpretation

It is clear that some line ratios are strong tracers of ISM conditions. A high $[\text{OIII}]\lambda 5007 / [\text{OIII}]\lambda 4959$ or $[\text{NeIII}]\lambda 3968 / [\text{NeIII}]\lambda 3869$ ratio

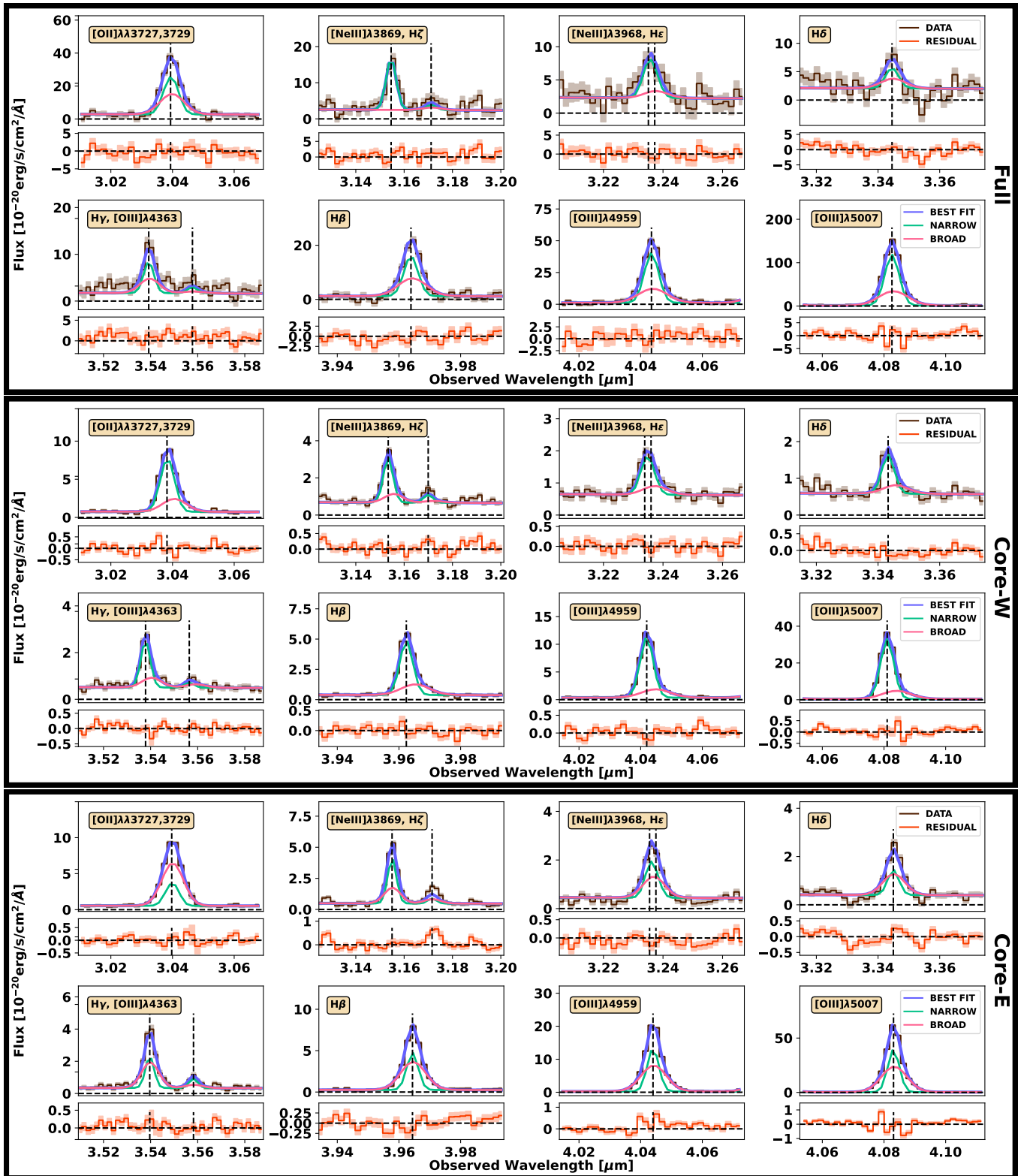


Figure C1. Spectra extracted from our JWST/NIRSpec IFU data cube using the apertures shown in Figure 2. For each region, we zoom in around each emission line and present the observed spectrum, the best-fit model, and its narrow and broad components. The residual is included in the lower panel. The redshifted wavelengths of each fit line (using the best-fit redshift of the narrow component) are marked with vertical dashed lines.

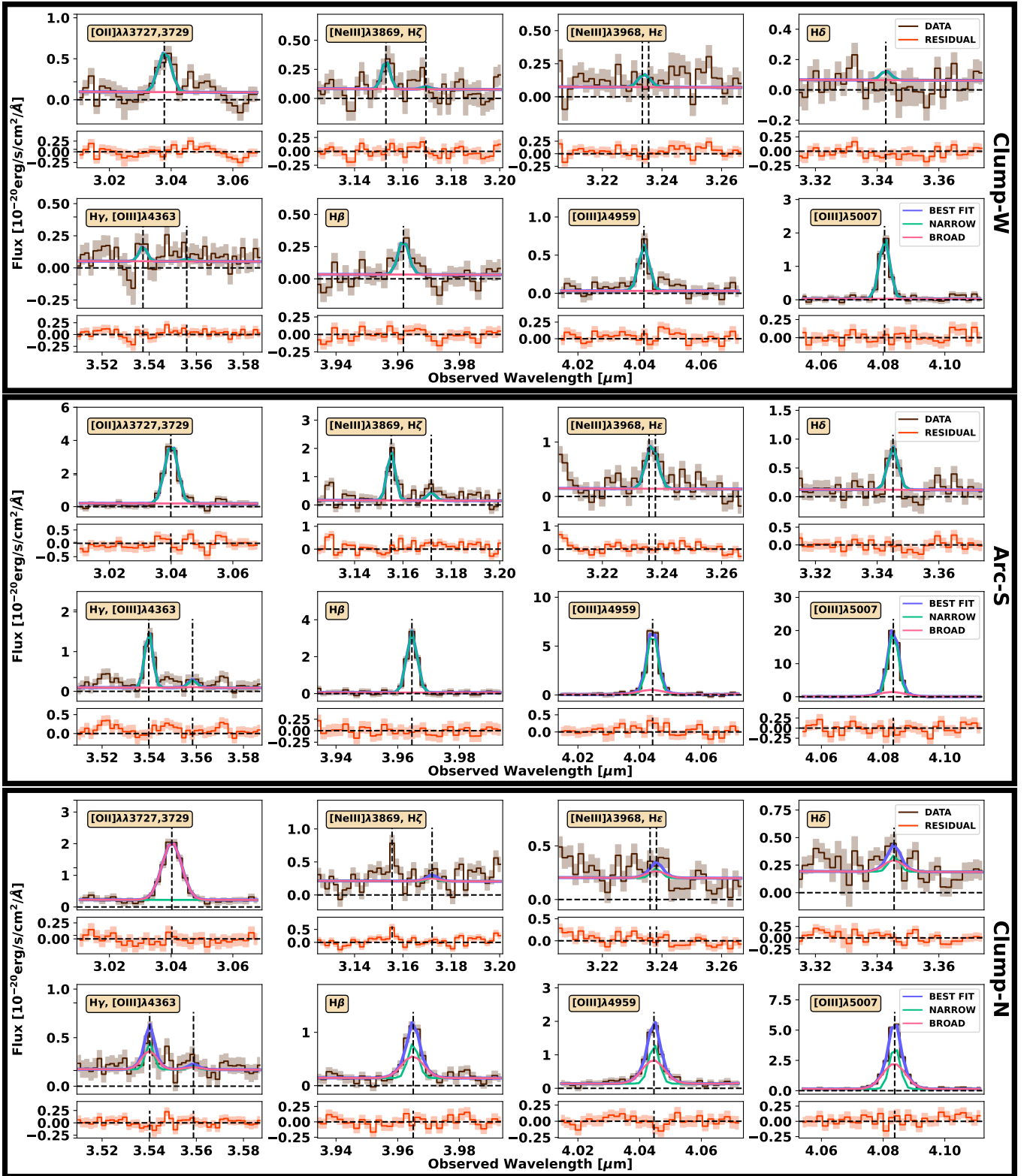


Figure C1. (Cont.)

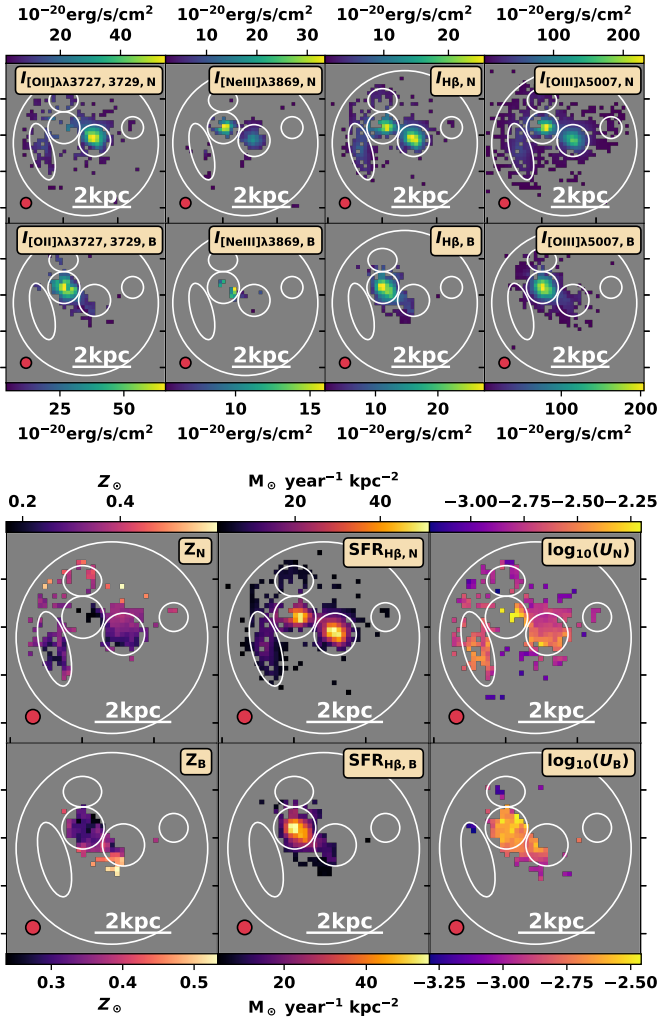


Figure D1. Integrated fluxes of emission lines (top panels) and line diagnostics (bottom panels), as derived through spaxel-by-spaxel fit. Each panel displays a field of view of $2'' \times 2''$ centred on $10\text{h}01\text{m}40.68\text{s} + 1^\circ 54' 52.39''$. A physical scale bar of 2 kpc scale bar is included to the lower right in each panel. For each, we show the PSF as a red ellipse to the lower left. North is up and east is to the left.

implies strong dust reddening, while in the absence of reddening a low $[\text{OIII}]\lambda 3729/[\text{OIII}]\lambda 3726$ ratio will suggest a high electron density, and a high Balmer ratio (e.g., $\text{H}\gamma/\text{H}\beta$) traces a high electron temperature. But there is some ambiguity between n_e , T_e , and $E(B - V)$, as shown by the curved lines of constant ratio in Figures E1 and E2.

While $[\text{OIII}]\lambda 5007/[\text{OIII}]\lambda 4959$ and $[\text{NeIII}]\lambda 3968/[\text{NeIII}]\lambda 3869$ appear to be good tracers of $E(B - V)$, their small wavelength separations result in small changes in the observed ratio (e.g., $\lesssim 1\%$ for $E(B - V) \lesssim 0.5$) which would require high-S/N observations to constrain. In addition, we have assumed case B recombination here, while case A recombination would result in altered Balmer ratios (e.g., Scarlata et al. 2024). We fit each observed profile in this work with two components (i.e., narrow and broad), adding an additional complication to ratio interpretation.

Because of these features, our model returned poorly constrained results when $E(B - V)$ was allowed to vary. This was investigated further by repeating the fits, but fixing $E(B - V)$ to a range of values (i.e., 0.0, 0.1, 0.2, ..., 1.0) and comparing the resulting goodness of

fit (i.e., χ^2). The ‘Full’, ‘Core-E’, and ‘Arc-S’ spectra were best fit with $E(B - V) = 0.0$, while ‘Core-W’ was best fit with $E(B - V) = 0.2$. The two weaker clumps (‘Clump-W’ and ‘Clump-N’) were best fit with higher colour excesses (0.6 and 0.4, respectively), but this may be simply due to low-amplitude lines. This simple test suggests that the attenuation of the ionised gas is low in the cores (i.e., $\lesssim 0.2$), and may be stronger in Core-W than in Core-E (i.e., the inverse of the relationship found for stellar continuum attenuation by Sugahara et al. 2024).

With these notes in mind, we make several assumptions for our fitting procedure. First, since we lack any strong tracers of n_e (i.e., the spectral resolution to resolve the $[\text{OIII}]\lambda\lambda 3726, 3729$ doublet), we fix n_e to the fiducial value of 200 cm^{-3} used by Sugahara et al. (2024). Next, we conservatively fix $E(B - V)$ to the value found by Sugahara et al. (2024) for the full B14-65666 system (0.2). Finally, we assume that for each component, each line may be characterised by the same ISM conditions (n_e , T_e , and $E(B - V)$), and include T_e as a variable in each fit.

This paper has been typeset from a $\text{\TeX}/\text{\LaTeX}$ file prepared by the author.

